



CENTRO DE INVESTIGACIONES
EN OPTICA, A.C.

**“SURFACE MEASUREMENT WITH VERTICAL
SUPER-RESOLUTION OF ALUMINUM THIN FILMS BY
USING PHASE-SHIFTING INTERFEROMETRY”**



**In partial fulfillment of the requirements for the degree of
Doctor of Science (Optics)**

Presented by: Jovanetty Ivan Choque Aquino

Advisor: Dr. Manuel Servin Guirado

***León · Guanajuato · México
May 2021***

Surface measurement with vertical super-resolution of aluminum thin films by using phase-shifting interferometry

A DISSERTATION PRESENTED

BY

Jovanetty Ivan Choque Aquino

IN PARTIAL FULFILLMENT OF THE REQUIREMENTS

FOR THE DEGREE OF

Doctor of Science (Optics)

MAY 2021

For you because you are the star that illuminates all my hopes.

Acknowledgments

I would like to thank the following people, without whom I would not have been able to complete this work, and without whom I would not have made it through my Ph.D. degree.

First of all, I would like to express my sincere gratitude to the Mexican National Council of Science and Technology (CONACYT) for awarding me a Ph.D. scholarship.

I would like to thank my advisor, Dr. Manuel Servin, for his continuous support, for his patience, and for his immense knowledge. His guidance helped me throughout the researching and writing of this dissertation. I certainly made the best decision when I asked him to be my advisor.

Besides my advisor, I would like to thank the rest of my working group: Dr. Moises Padilla, MSc. Sotero Ordonez, and MSc. Guillermo Garnica, for their insightful comments and criticism, but also for their hard questions which aroused me to widen my vision from different perspectives.

I am indebted to professor Guillermo Baldwin and MSc. Miguel Asmad for research facilities at Pontificia Universidad Catolica del Peru (PUCP). They gave me access to use the Michelson interferential microscope and to collect interferometric data, without their valuable support, it would not be possible to accomplish this dissertation.

I thank my friends: Azael, Daniel Luis, Daniel Alexis and Natalith for all the unconditional support in this very intense academic experience at CIO, for the stimulating discussions, for the sleepless nights we worked together before deadlines, and for all the fun we have had in the last three years.

Last but not least, I would like to thank my family: Mario, Domitila, Diego, Betty, Dayber, Maritza and Sebastián who generate an atmosphere of love, happiness and hope.

Surface measurement with vertical super-resolution of aluminum thin films by using phase-shifting interferometry

ABSTRACT

In this dissertation, we present a procedure to measure the phase from non-uniform phase-shifting interferograms in order to estimate the surface topography of an aluminum thin film. Interferograms are acquired from a Michelson interferential microscope, and phase shifts among interferograms are non-uniform because a piezoelectric transducer (PZT), working in open-loop mode, is used as phase shifter. Non-uniform phase shifts generate two types of errors in phase measurements: the double-frequency ripple distortion and the spurious piston. Thus, in order to overcome the aforementioned errors, we design error-correcting and non-iterative phase shifting algorithms (PSAs). For this purpose, considering that non-uniform phase shifts can be expressed as a polynomial function of the unperturbed phase shift (ω_0) and using the frequency transfer function (FTF) formalism, we show that the conditions to overcome errors in phase measurements are associated with m -th derivative of the PSA's FTF. Hence, we deduce two new conditions: 1) the m -th derivative of the FTF evaluated at $\omega = -\omega_0$ to suppress the double-frequency ripple distortion, and 2) the m -th derivative of the FTF evaluated at $\omega = \omega_0$ to eliminate the spurious piston. Then, taking into account the m -th derivative of the FTF evaluated at $\omega = -\omega_0$, we design a nine-frame PSA in order to estimate the surface topography of an aluminum thin film. This result is free of ripple distortions and it is better than those obtained using the Fourier transform method, the least-squares PSA, and the principal component analysis method. Finally, we applied our nine-frame PSA to three different sets of non-uniform phase-shifting interferograms. Demodulated phases are summed in order to obtain a phase with vertical super-resolution (Vertical sensitivity), equivalent to measure surfaces with a synthetic ultraviolet wavelength. Computer simulations and experimental results prove us right.

Contents

I	INTRODUCTION	I
1.1	Motivation	2
1.2	Research problem	2
1.3	Objectives	3
1.4	Hypothesis	4
1.5	Dissertation contents	4
2	THEORETICAL FRAMEWORK	5
2.1	Two-beam interference	5
2.2	Phase shifting interferometry	8
2.3	Phase-shifting algorithm	9
2.4	Figures of merit of PSA	11
2.5	From wavefront to surface	14
3	AVOIDING ERRORS IN PHASE MEASUREMENT	15
3.1	Error sources in PSI	15
3.2	Mathematical analysis	17
3.3	Enhanced four-frame PSA	19
3.4	Simulation results	23
3.5	Discussions	25
4	SURFACE TOPOGRAPHY OF ALUMINUM THIN FILM	27
4.1	Groundwork	27
4.2	Phase shifts measurement	28
4.3	Modified phase shifting interferogram	30
4.4	A custom-made nine-frame PSA	31
4.5	Experimental results	32

5	SURFACES WITH VERTICAL SUPER-RESOLUTION	35
5.1	Multiple wavelength in PSI	35
5.2	Groundwork	37
5.3	Experimental results	38
5.4	Discussion	39
6	CONCLUSIONS AND FUTURE WORKS	41
6.1	Conclusions	41
6.2	Future works	43
	APPENDIX A THE CHARACTERISTIC POLYNOMIAL OF PSAs	44
	APPENDIX B PHASE UNWRAPPING	46
	APPENDIX C PUBLISHED MATERIAL	48
	REFERENCES	50

List of figures

2.1	Two-beam interference between a flat reference wavefront (a), which is tilted α about the x -axis, and a wavefront under analysis $W(x, y)$ (b).	6
2.2	Michelson interferential microscope setup.	7
2.3	Shifting the phase in the Michelson interferential microscope by moving the specimen surface.	9
2.4	A set of phase-shifting interferograms.	9
2.5	(a) Spectrum of the temporal phase shifting interferogram. (b) Frequency transfer function of an ideal quadrature (band-pass) linear filter.	10
2.6	FTF magnitude of the Four-Frame PSA (blue line), and the Schwider-Hariharan PSA (red line). Temporal phase shifting interferogram (black line).	12
2.7	Normalized-frequency spectral plot, $ H(\omega) $ versus ω/ω_0 , to assess the harmonic rejection capability of the four-frame PSA and Schwider-Hariharan PSA. Rejected harmonics are represented by blurred dashed arrows.	13
2.8	Phase diagram of the true analytic signal and the estimated analytic signal in phase demodulation.	14
3.1	Uniform (blue line) and non-uniform (red line) phase-shift distributions. (a) Absolute phase shifts and (b) phase shift differences between two consecutive interferograms.	16
3.2	Magnitude (red line) and phase (blue line) of the FTF of (a) four-frame PSA, (b) six-frame PSA, and (c) eight-frame PSA.	22
3.3	Roots position of (a) four-frame PSA, (b) six-frame PSA, and (c) eight-frame PSA.	23
3.4	Eight simulated interferograms used as input data for phase demodulation. . .	24
3.5	Phase map measured by using (a) four-frame PSA, (b) six-frame PSA, and (c) eight-frame PSA.	24

3.6	Phase errors computed from (a) noiseless interferograms and (b) interferograms corrupted by AWGN with $\sigma = 3$	25
4.1	Nine ($N = 9$) phase shifting interferogram acquire from Michelson interferential microscope. Information of the aluminum thin film is encoded into the interferometric fringes.	28
4.2	Uniform (blue line) and non-uniform (red line) phase-shift distributions. (a) Sequential phase shifts and (b) phase-shift differences among consecutive interferograms.	29
4.3	Spectrum of (a) non-uniform and (b) modified phase shifting interferogram.	31
4.4	(a) Spectrum of the modified non-uniform phase-shifting interferogram (black line) superposed by the FTF magnitude of nine-frame PSA (blue line). (b) Root positions of its corresponding characteristic polynomial.	32
4.5	Height map using (a) Fourier method, (b) eight-step frequency-shifted LS-PSA, (c) PCA method, and (d) proposed algorithm.	33
4.6	Vertical slices of the estimated surfaces using Fourier method (red line), eight-step frequency-shifted LS-PSA (black line), PCA method (blue line), and proposed algorithm (green line).	34
5.1	(a) Phase map measured at wavelength of $\lambda_1 = 660$ nm. Phase map measured at synthetic equivalent wavelength of (b) $\lambda_{s2} = 330$ nm, and (c) $\lambda_{s3} = 220$ nm.	38
5.2	Surface topography of aluminum thin film using phase-sum at equivalent wavelength $\lambda_{eqs} = 220$ nm.	39
5.3	Phase map measured at wavelength of (a) $\lambda_1 = 660$ nm and (b) $\lambda_2 = 530$ nm. Phase measured at synthetic equivalent wavelength of $\lambda_{s12} = 293.95$ nm.	39
5.4	Surface topography of aluminum thin film using phase-sum at equivalent wavelength $\lambda_{eqs} = 293.95$ nm.	40
A.1	Roots position of (a) the Four-Frame PSA and (b) the Schwider-Hariharan PSA.	45
B.1	Phase unwrapping in fringe analysis. In red line the wrapped phase and in blue line the unwrapped phase.	47

List of Tables

2.1	Figures of merits for four-frame PSA and Schwider-Hariharan PSA.	13
3.1	Figures of merits for four-frame PSA, six-frame PSA, and eight-frame PSA. . .	23
3.2	Computed root-mean-square (<i>rms</i>) errors and peak-to-valley (<i>p-v</i>) errors by the four-frame PSA, six-frame, and eight-frame PSA.	26
4.1	Figures of merits for the proposed nine-frame PSA.	33

1

Introduction

In order to measure the phase in phase-shifting interferometry (PSI), numerous phase-shifting algorithms (PSA) have been reported [1–10]. Most PSAs consider that the phase shifts among interferograms vary in known manner and constant, this is known as uniform phase shift. However, in practical measurements, interferometric data has a different phase shift than the expected value; these are called non-uniform phase shifts. Therefore, errors in the measured phase are introduced when interferograms with non-uniform phase shifts are processed using conventional algorithms.

Non-uniform phase shifts arise due to most PSI setups use a piezoelectric transducer (PZT) as phase shifter [11]. It is known that phase shifts based on PZT displacement are non-linear [4, 11–13], and they have poor repeatability [4, 14]. Besides the PZT, atmospheric turbulence [15] and mechanical vibration [16–21] also introduce additional phase shift uncertainties. Ai and Wyant sum up non-uniform phase shift as linear and quadratic terms [11], whereas Hibino *et al.* proposed that the non-uniform phase shifts can be approximated by a polynomial function of the unperturbed phase shift value and nonlinear coefficients [10, 22–24].

It is well known that nonuniform phase shifts cause double-frequency ripple distortions [11, 12, 25]. In some cases, ripple distortions can be suppressed by error-correcting PSAs designed for uniform phase shifts [3, 4, 6, 26]. However, in other cases, it is necessary to use more robust approaches such as the principal component analysis (PCA) [27–30], the advanced iterative al-

gorithm (AIA) [31], or VU factorization [32]. Nonetheless, the optical phase computed by the aforementioned PSAs may include a spurious piston [24, 33]. In most cases, this spurious piston is irrelevant. However, it can be a problem in absolute phase measurements such as optical thickness [34] and air gap distance [35], in which it can be wrongly interpreted as a real physical quantity.

In this dissertation, we present error-correcting, and ready-to-use PSAs in order to measure the surface topography of an aluminum thin film. PSAs are designed from the point of view of the frequency transfer function (FTF) and they are robust against the two phase measurement errors: the double-frequency ripple distortion and the spurious piston.

1.1 MOTIVATION

There are materials research groups who are interested in measuring the thickness, roughness, and singularities of thin films. In the specific case of aluminum thin films, which are extremely sensitive to contamination, soft and easily deformed specimens, it is desirable to use an accuracy instrument which does not make contact with the specimens. In that sense, phase shifting interferometry technique is the best option, because it is a non-destructive method and it provides accuracy and precision, in the nanometer or even the Angstrom range [36].

Despite of the aforementioned, PSI is not necessarily a very high precision technique because conventional PSAs used for phase retrieval in PSI carries two intrinsic errors: the double-frequency ripple distortion and the spurious piston. Therefore, measuring thickness and roughness by using PSI is not reliable because PSI is too sensitivity to phase shifting variations and operating conditions of the interferometer. In that sense, these errors have to amend and it give us a opportunity to research and to improve the conventional PSAs.

Nonetheless, our enhanced PSAs can be used in numerous industrial, research and development applications. These include measuring the quality of a variety of manufactured items, such as hard disk drives and magnetic recording heads, lasers and optics for CD and DVD drives, cameras, laser printers, machined parts and components for fiber-optic systems[37].

1.2 RESEARCH PROBLEM

As discussed, PZT displacement produces interferometric data with non-uniform phase shifts. Processing it without robust methods translates into a double-frequency ripple distortion and a spurious piston; both errors can be easily interpreted as physical quantities, resulting in wrong measurements. This dissertation proposes PSAs to avoid errors in phase measurements.

This dissertation does not propose to improve the environmental condition nor to adjust the

PZT displacement. On the contrary, we work on the fact that the phase shifts are non-uniform. Thus, our research is focused on designing error-correcting and non-iterative PSAs in order to avoid errors in the measured phase. PSAs design process involve the m -th derivative of the PSA's frequency transfer function, first, evaluated at $\omega = -\omega_0$ to suppress the double-frequency ripple distortion, and second, evaluated at $\omega = \omega_0$ to eliminate the spurious piston. These conditions help us to design enhanced PSAs which are robust against errors in phase measurement, and it result in more accurate measurements.

Thin films properties and manufacturing will not be discussed in this dissertation.

1.3 OBJECTIVES

1.3.1 GENERAL OBJECTIVE

To measure the surface topography of an aluminum thin film using a custom-made phase shifting algorithm.

1.3.2 SPECIFIC OBJECTIVES

- To illustrate the non-uniform phase shift in experimental data acquired from the Michelson interferential microscope.
- To deduce conditions, from the point of view of the frequency transfer function, to design phase shifting algorithms in order to suppress the double-frequency ripple distortion and to eliminate the spurious piston.
- To show the evolution of the well-known four-frame PSA, which can be modified in order to avoid errors in the measured phase.
- To design a custom-made PSA in order to measure the surface topography of an aluminum thin films using interferograms with non-uniform phase shifts.
- To compare the obtained surface topography of an aluminum thin films with similar phase shifting algorithms.
- To estimate the surface topography of an aluminum thin film with vertical super-resolution by using ultraviolet equivalent-wavelength PSI.

1.4 HYPOTHESIS

A custom-made phase shifting algorithm, from the point of view of the frequency transfer function, allows us to deduce conditions in order to suppress two common phase errors, the double-frequency ripple distortion and the spurious piston. This algorithm permit us to measure an error free 3-D map of aluminum thin film surface.

1.5 DISSERTATION CONTENTS

The theoretical framework is presented in Chapter 2. Theoretical foundations about two beam interference, phase-shifting interferometry, phase-shifting algorithm from the point of view of the frequency transfer function, and figures of merits of PSA are studied. This chapter includes a description of the Michelson interferential microscope.

Conditions to avoid errors in phase measurement are deduced in Chapter 3. This Chapter starts giving a overview of the error sources in PSI. Then, mathematical analysis to deduce two conditions: one to suppress the double-frequency ripple distortion, and other to eliminate the spurious piston are developed. The two proposed conditions are applied over the well-known four-frame PSA. Lastly, simulation results show the validity of our proposal.

An experimental process to estimate the surface topography of an aluminum thin film is carried out in Chapter 4. This chapter starts remembering that a non-uniform phase shift is composed by a nominal value and a phase shift error. Then, processes to estimate the phase shift error, to define a modified phase-shifting interferogram, and to design a error-correcting nine-frame PSA are explained. Lastly, 3-D surfaces topography of an aluminum thin film are shown.

Procedures to estimate the surface topography of an aluminum thin film with vertical super-resolution is carried out in Chapter 5. This chapter describes the process to demodulate the phase from several sets of non-uniform phase shifting interferograms. Demodulated phases are summed in order to obtain a new phase map which has ultraviolet sensitivity, as if it was measured using a light source with ultraviolet wavelength.

Finally, our conclusions are drawn in Chapter 6. At the same time, this chapter gives an outlook about future works.

2

Theoretical framework

In this chapter, we describe in detail the elements of *phase shifting interferometric* (PSI) for optical testing, this technique is mainly based on the phenomena of interference and phase shifting algorithms (PSA). It will be described with principal reference to applications for the topographic measurements of thin films.

2.1 TWO-BEAM INTERFERENCE

Two-beam interference is the coherent superposition of two wavefronts [38–40], one of which is typically a flat reference wavefront that has a tilt, e.g. about the x -axis

$$E_1(x, y) = E_{01}(x, y)e^{ikx \sin \alpha}, \quad (2.1)$$

and the other a wavefront under analysis, whose shape is to be measured

$$E_2(x, y) = E_{01}(x, y)e^{ikW(x, y)}. \quad (2.2)$$

Here, $W(x, y)$ represent deformations with respect to a flat wavefront without tilt [41]. These wavefronts are shown in Fig. 2.1.

The complex amplitude in the observation plane, where the two wavefronts interfere, is given

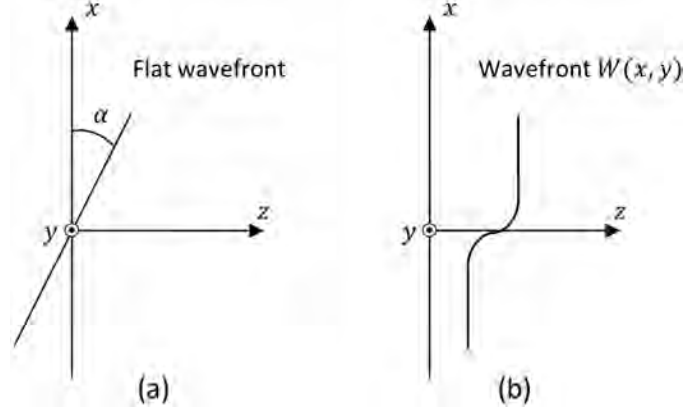


Figure 2.1: Two-beam interference between a flat reference wavefront (a), which is tilted α about the x -axis, and a wavefront under analysis $W(x, y)$ (b).

by

$$E(x, y) = E_{01}(x, y)e^{ikx \sin \alpha} + E_{02}(x, y)e^{ikW(x, y)}, \quad (2.3)$$

where E_{01} is the amplitude of the light beam with the reference wavefront, E_{02} is the amplitude of the light beam at the wavefront under analysis, $k = 2\pi/\lambda$, and λ is the wavelength of light.

The optical disturbance, or electric field \vec{E} , varies in time at an exceedingly rapid rate, roughly 4.3×10^{14} Hz to 7.5×10^{14} Hz [42], this made the actual field an impractical quantity to detect.

The study of interference is best approached by way of the irradiance, because it can be measured directly with a wide variety of sensors, such as photocells, bolometers, photographic emulsions, or eyes. Irradiance is defined by

$$I(x, y) = E(x, y) \cdot E^*(x, y), \quad (2.4)$$

here the symbol $*$ denote the complex conjugate of the electric field.

Substituting Eq. (2.3) into Eq. (2.4), we have

$$\begin{aligned} I(x, y) &= E_{01}^2(x, y) + E_{02}^2(x, y) \\ &\quad + 2E_{01}(x, y)E_{02}(x, y) \cos k[W(x, y) - x \sin \alpha]. \end{aligned} \quad (2.5)$$

Then, the irradiance function $I(x, y)$ is given by

$$\begin{aligned} I(x, y) &= I_1^2(x, y) + I_2^2(x, y) \\ &\quad + 2\sqrt{I_1(x, y)I_2(x, y)} \cos k[W(x, y) - x \sin \alpha], \end{aligned} \quad (2.6)$$

where $I_1(x, y)$ and $I_2(x, y)$ are the irradiances of the two beams, and the phase difference between

them is given by $\phi(x, y) = k[W(x, y) - x \sin \alpha]$, where the term in square brackets is known as optical path difference (*OPD*). Phase difference can be rewritten as

$$\phi(x, y) = \varphi(x, y) - u_0 x. \quad (2.7)$$

Here $\varphi(x, y)$ and $u_0 x$ are phases corresponding to the specimen surface and the tilted reference plane, respectively. In this case, u_0 is the spatial carrier in the x direction [43].

For practical purposes, Eq. (2.6) is written as [41]

$$I(x, y) = a(x, y) + b(x, y) \cos [\phi(x, y)], \quad (2.8)$$

where $a(x, y)$ and $b(x, y)$ are known as the background illumination and the local contrast function, respectively; and $\phi(x, y)$ is the searched phase which is proportional to the phenomenon under study. From now on for simplicity, the arguments x and y will be omitted.

Among the various types of two-beam interferometers, the *Michelson interferometer* is especially simple and straightforward in principle, as well as in practice, and is therefore utilized for a broad range of applications. This interferometer has several variants, e.g. the Michelson interferential microscope.

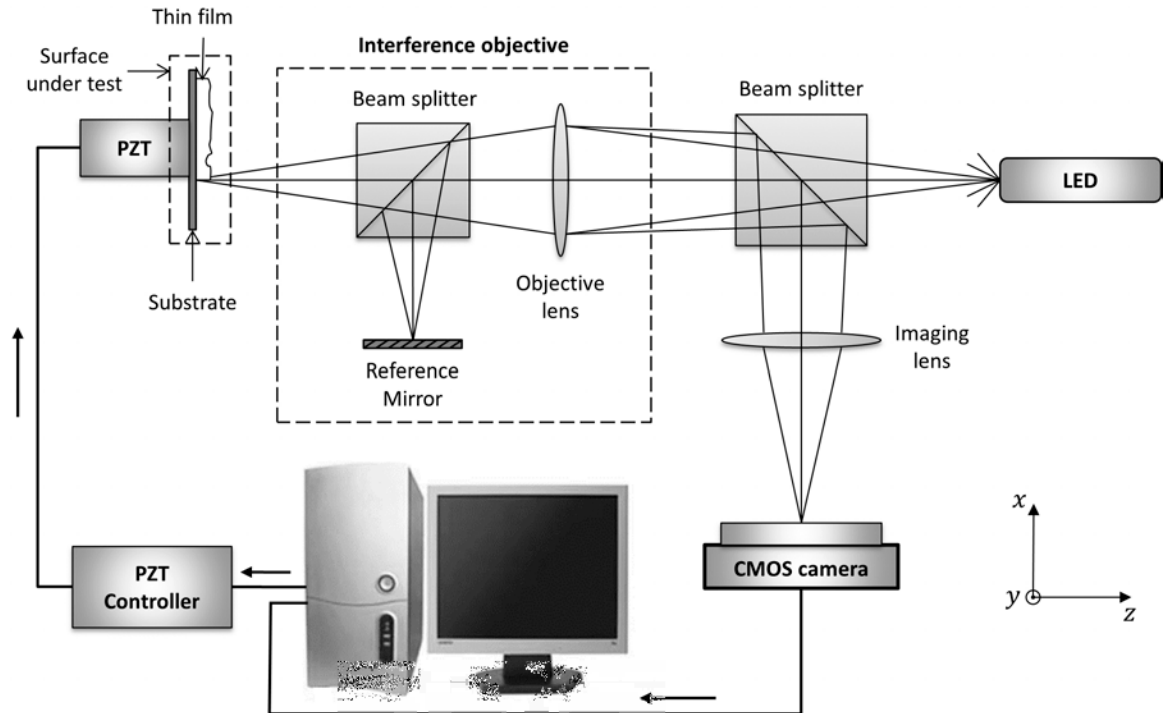


Figure 2.2: Michelson interferential microscope setup.

Figure 2.2 shows the Michelson interferential microscope for testing the surface and thickness of an aluminum thin film sample. The source is a high-power LED that has a dominant

wavelength of $\lambda = 660$ nm. The beam is transmitted and divided into two by an external beam splitter: one goes to an interference objective with a magnification of $5\times$ [36] and $NA = 0.13$; and the other is not a subject of interest. Once inside the interference objective, the transmitted beam is split into two beams of nearly equal intensity by an internal beam splitter; one of these beams is directed onto a flat reference mirror and the other onto the specimen surface. Since the light waves reflected by the specimen and the reference mirror are originated from the same light source, these waves are mutually coherent, and consequently a two-beam interference pattern is obtained. The image of the surface under test, superimposed with interference fringes, is directed towards to an image lens by the external beam splitter. The generated two-beam interference pattern is registered by a CMOS camera.

The interference objective and specimen surface are separated by an appreciable distance (≈ 9 mm), as shown in Fig. 2.2. Therefore, an interference pattern is obtained without contact. This is suitable in the case of specimens such as semiconductors, which are extremely sensitive to contamination, or soft and easily deformed specimens [36].

In this dissertation, aberrations due to anything that both beams go through, such as the imaging lens or the beam splitter, are negligible in fringe pattern analysis. Therefore, interferograms represent only the difference between the two interfering beams. [44].

2.2 PHASE SHIFTING INTERFEROMETRY

Shifting the specimen surface in the z -axis positive direction has the effect of varying the phase difference between the two beams which are interfering. One way to vary the phase difference is to apply a voltage to a piezoelectric transducer (PZT) on which the specimen surface is mounted, see Fig. 2.3. This surface is moved in several discrete steps, and then taken and stored the interferometric data in the computer before the surface moves to the next position [11]. During movement, N interferograms are recorded at an equal voltage interval, such that

$$\begin{aligned} I_n &= a + b \cos[\phi + \omega_0 n]; \\ n &= 0, \dots, N-1 \end{aligned} \tag{2.9}$$

Here, ω_0 is the temporal carrier, which represent the phase shift between two consecutive interferograms. A set of phase-shifting interferograms is shown in Fig. 2.4. From these interferograms, the searched phase ϕ can be derived from three or more interferograms [45]. This technique is known as phase shifting interferometry (PSI).

The most common value of ω_0 is $\pi/2$ (90°). In a Michelson interferential microscope, a phase shift of $\pi/2$ is equivalent to moving the surface under test $\lambda/8$, it means moving the specimen surface about 82.5 nm for each new interferogram ($\lambda = 660$ nm). In the same way, a shift

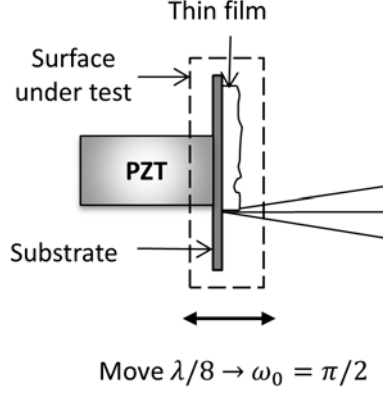


Figure 2.3: Shifting the phase in the Michelson interferential microscope by moving the specimen surface.

through one-fourth of a wavelength inverts the pattern by transforming bright fringes to dark fringes, and viceversa.

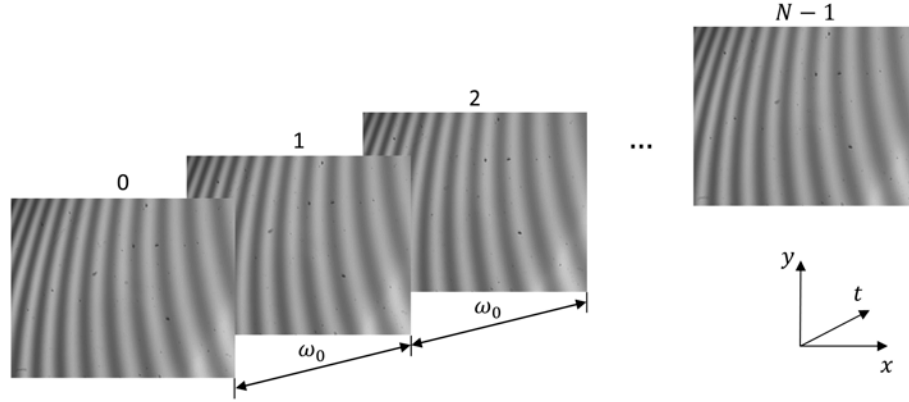


Figure 2.4: A set of phase-shifting interferograms.

2.3 PHASE-SHIFTING ALGORITHM

The mathematical representation of the phase-shifting interferogram, given by Eq. (2.9), can be rewritten in a continuous-time model as

$$I(t) = a + \frac{1}{2}be^{i[\phi+\omega_0 t]} + \frac{1}{2}be^{-i[\phi+\omega_0 t]}. \quad (2.10)$$

The temporal Fourier transform of the $I(t)$ is given by

$$I(\omega) = a\delta(\omega) + \frac{b}{2}e^{i\phi}\delta(\omega - \omega_0) + \frac{b}{2}e^{-i\phi}\delta(\omega + \omega_0). \quad (2.11)$$

The above equation means that the temporal carrier modulation produces spectral separation between the component signals of the interferogram. Taking account that a , b , and ϕ do not

have temporal dependency, the spectral lobes are given by Dirac delta functions located at $\omega = \{-\omega_0, 0, \omega_0\}$, as shown in Fig. 2.5(a).

Equation (2.11) allows us to design a proper linear filter to chose the analytical signal $(b/2) \exp[i\phi]$ located at $\omega = \omega_0$ and to reject the other ones, as shown in Fig. 2.5(b). Readers must note that it is also valid choosing the signal located at $\omega = -\omega_0$.

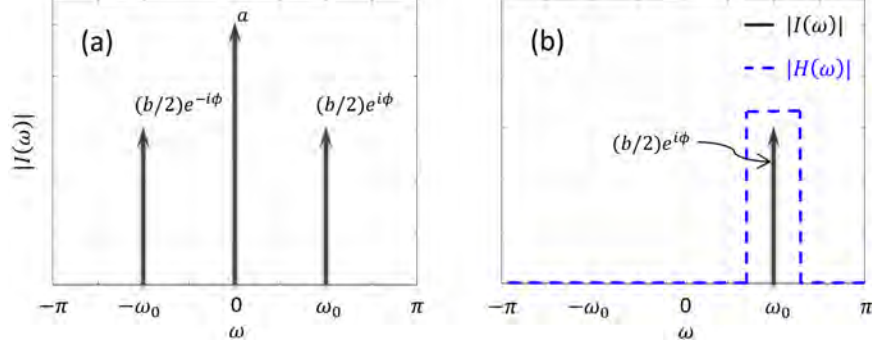


Figure 2.5: (a) Spectrum of the temporal phase shifting interferogram. (b) Frequency transfer function of an ideal quadrature (band-pass) linear filter.

In the Fourier domain, a quadrature linear filter is completely characterized by its frequency transfer function (FTF) [43]

$$H(\omega) = \sum_{n=0}^{N-1} c_n e^{-i\omega n}, \quad (2.12)$$

where c_n are complex-valued coefficients that define $H(\omega)$.

Now, in order to isolate the analytical signal $(b/2) \exp[i\phi]$, the FTF must fulfill the following quadrature conditions:

$$H(0) = 0, \quad H(-\omega_0) = 0, \quad H(\omega_0) = 1. \quad (2.13)$$

Note that, for simplicity we are considering that $H(\omega_0) = 1$, nonetheless, this can be any positive real nonzero value.

Applying this quadrature linear filter to Eq. (2.11), in the Fourier domain, we have

$$I(\omega)H(\omega) = \frac{b}{2}H(\omega_0)e^{i\phi}\delta(\omega - \omega_0). \quad (2.14)$$

This procedure is translated to the time domain by using the impulse response function

$$\mathcal{F}^{-1}\{H(\omega)\} = h(t) = \sum_{n=0}^{N-1} c_n \delta(t - n). \quad (2.15)$$

In similar way, but in the time domain, applying the quadrature linear filter $b(t)$ to the temporal phase-shifting interferogram $I(t)$, we have

$$[I(t) \otimes b(t)]_{t=N-1} = \sum_{n=0}^{N-1} c_n I_n, \quad (2.16)$$

where \otimes denotes the convolution operator. Note that in Eq. (2.16), the temporal convolution is evaluated at $t = N - 1$ in order to obtain the most robust estimation of the analytic signal for a given number of phase steps. So, for practical purposes, Eq. (2.16) can be written as

$$\frac{\hat{b}}{2} e^{i\hat{\phi}} = \sum_{n=0}^{N-1} c_n I_n. \quad (2.17)$$

Thus, the searched phase ϕ , modulo 2π , is easily computed as the argument of this analytic signal

$$\hat{\phi} = \arg \left\{ \frac{\hat{b}}{2} e^{i\hat{\phi}} \right\}. \quad (2.18)$$

For the aforementioned, a *phase-shifting algorithm* (PSA) can be described as quadrature linear filter. In that sense, the two most representatives PSAs, Four-Frame [2] and Schwider-Hariharan [3, 4], can be expressed by their analytic signals [43]

$$\frac{\hat{b}}{2} e^{i\hat{\phi}_{FF}} = I_0 - iI_1 - I_2 + iI_3, \quad (2.19)$$

$$\frac{\hat{b}}{2} e^{i\hat{\phi}_{SH}} = I_0 - 2iI_1 - 2I_2 + 2iI_3 + I_4. \quad (2.20)$$

Figure 2.6 shows the FTF magnitude of the Four-Frame PSA (blue line) and Schwider-Hariharan PSA (red line). Note that these PSAs are similar behavior to isolate the analytical signal $(b/2) \exp[i\phi]$. However, in Schwider-Hariharan PSA $H(\omega) \approx 0$ around $\omega = -\omega_0$, it does not observe in Four-Frame PSA. This remarkable difference will be discussed in the following two chapters.

2.4 FIGURES OF MERIT OF PSA

One important advantage of using the FTF formalism is to obtain the figures of merit of a PSA. Figures of merit are indicators to measure the reliability of PSAs against common error sources such as additive random noise and distorting harmonics.

2.4.1 SIGNAL-TO-NOISE RATIO GAIN

In order to analyze the robustness of PSAs, we must analyze their behavior against noise. Typically, it is assumed that the interferometric data is being distorted by a zero-mean Additive white

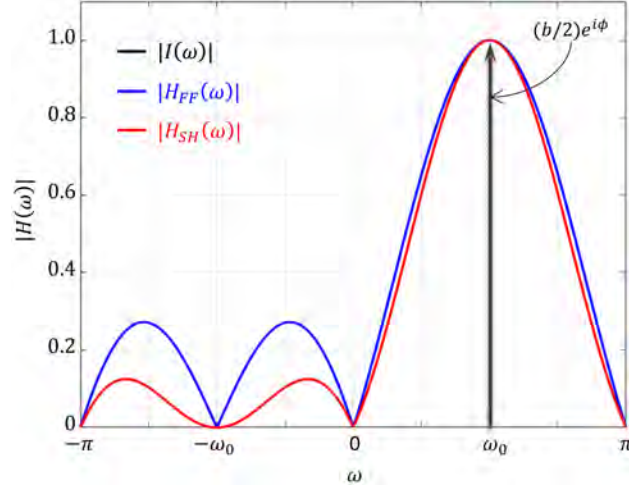


Figure 2.6: FTF magnitude of the Four-Frame PSA (blue line), and the Schwider-Hariharan PSA (red line). Temporal phase shifting interferogram (black line).

Gaussian noise (AWGN) with flat power $\eta_0/2$. Then, the signal-to-noise ratio (SNR) for the demodulated signal is given by [43]

$$SNR = \frac{(b_1^2/4)}{(\eta/2)} \left[\frac{\left| \sum_{n=0}^{N-1} c_n e^{in\omega_0} \right|^2}{\sum_{n=0}^{N-1} |c_n|^2} \right]. \quad (2.21)$$

The term in squared brackets depends only of the PSA's coefficients. It is called the SNR gain of PSA:

$$G_{SNR} = \frac{\left| \sum_{n=0}^{N-1} c_n e^{in\omega_0} \right|^2}{\sum_{n=0}^{N-1} |c_n|^2}, \quad 0 < G_{SNR} < N. \quad (2.22)$$

The optimal gain ($G_{SNR} = N$) corresponds to least-squares PSA proposed by Bruning et al [1].

2.4.2 HARMONICS REJECTION

Distorting harmonics appear when the interferometric fringes have non-sinusoidal profiles. Then, the interferometric data can be modeled as

$$I_n = a + \sum_{k=1}^{\infty} b_k \cos[k(\phi + \theta_n)], \quad (2.23)$$

here b_k is the contrast function for the k -th harmonic ($b_k \ll b_1$), whereas all other terms have

been previously defined in section 2.1. Then, in order to isolate the $(b_1/2) \exp(i\phi)$ term, it requires additional FTF conditions, which are given by

$$H(\pm k\omega_0) = \sum_{n=0}^{N-1} c_n e^{\pm i k n \omega_0} = 0, \quad k \in \{2, 3, \dots\}. \quad (2.24)$$

An important thing to mention is that by introducing $H(\pm k\omega_0) = 0$, the G_{SNR} improves.

Figure 2.7 illustrates the harmonics rejection capability of the Four-Frame PSA and Schwider-Hariharan PSA. In both cases, within a normalized frequency range $\omega/\omega_0 = [-10, 10]$, these PSAs fail to reject the distorting harmonics $\{-7, -3, 5, 9\}$. Rejected harmonics are represented by blurred dashed arrows.

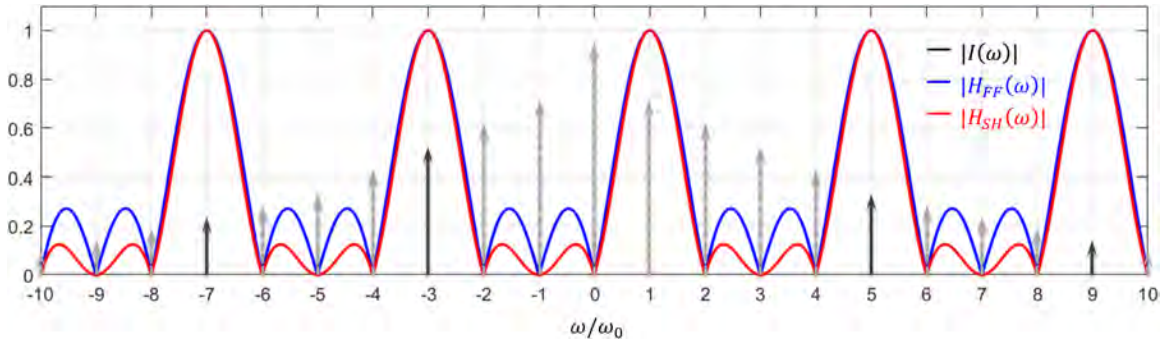


Figure 2.7: Normalized-frequency spectral plot, $|H(\omega)|$ versus ω/ω_0 , to assess the harmonic rejection capability of the four-frame PSA and Schwider-Hariharan PSA. Rejected harmonics are represented by blurred dashed arrows.

Table 2.1 resumes the figures of merit of the four-frame PSA and Schwider-Hariharan PSA.

Table 2.1: Figures of merits for four-frame PSA and Schwider-Hariharan PSA.

PSA	N	ω_0	Coefficient c_n	Harmonics*	G_{SNR}
four-frame	4	$\pi/2$	$\frac{1}{4}\{1, -i, -1, i\}$	$-7, -3, 5, 9$	4
Schwider-Hariharan	5	$\pi/2$	$\frac{1}{8}\{1, -2i, -2, 2i, 1\}$	$-7, -3, 5, 9$	4.57

* It refers to non-rejected distorting harmonics within the normalized frequency range $\omega/\omega_0 = [-10, 10]$.

Beside of the signal-to-noise ratio gain and the harmonics rejection, there is another very important figure of merit: *robustness against detuning*, it will be discussed in detail in the following two chapters.

For the aforementioned, an accuracy phase measurement implies to use a suitable PSA, which must be robust against noise, distorting harmonics and detuning. Consequently, the correct choice of a PSA will reduce the difference between a estimated phase $\hat{\phi}$ and the true phase ϕ . This

can be better understood by the following relationship

$$\frac{\hat{b}}{2}e^{i\hat{\phi}} = \frac{b}{2}e^{i\phi} + \varepsilon. \quad (2.25)$$

Here 'hat' denotes estimated values; and ε is a complex number which groups magnitudes and phase errors associated to detuning, distorting harmonics and noise. This relationship is depicted, as phase diagram, in Fig. 2.8. Here σ_ϕ and $\sigma_{b/2}$ represent the standard deviation in the measurement of ϕ and $b/2$, respectively.

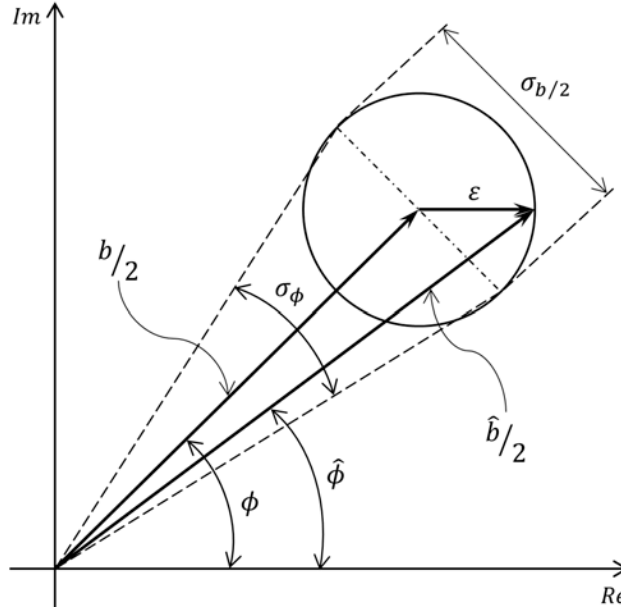


Figure 2.8: Phase diagram of the true analytic signal and the estimated analytic signal in phase demodulation.

2.5 FROM WAVEFRONT TO SURFACE

Once the phase is determined by using a PSA, the corresponding height distribution, $\mathcal{W}(x, y)$, on the test surface can be easily deduced from Eq. (2.7) [46]. But, the measured phase include two phases, $\varphi(x, y)$ and u_0x , so in order to calculate the searcher phase $\varphi(x, y)$, the spatial carrier u_0x must be removed. Thus, the corresponding height distribution across the interference field is given by

$$\mathcal{W}(x, y) = \frac{\lambda}{4\pi} \hat{\phi}(x, y). \quad (2.26)$$

This relation is valid for a double-pass interferometer like a Michelson type interferometer [44]. For single-pass interferometers, the denominator is 2π instead of 4π .

3

Avoiding errors in phase measurement

In this chapter, we deduce explicit conditions to design PSAs in order to avoid errors in phase measurement, the double-frequency ripple distortion and the spurious piston. We start giving a briefly overview about the relationship between error sources in PSI and interferograms with non-uniform phase shifts. Then, by modeling these non-uniform phase shifts as a polynomial function of the unperturbed phase shift value ω_0 , we expose that errors in phase measurement arise when non-uniform phase-shifting interferograms are processed with conventional PSAs, in the same way, we figure out that the conditions for eliminating those errors are associated with the m -th derivative of the PSA's FTF. Finally, our mathematical analysis is supported by computer simulations.

3.1 ERROR SOURCES IN PSI

The accuracy of most PSAs, e.g the well-known four-frames [2], relies critically on the precision of the phase shifts, which must vary in known manner and constant. However, phase shifts based on PZT have non linearity and poor repeatability. Moreover, an interferometer, e.g. the Michelson interferential microscope, and the specimen surface are exposed to atmospheric turbulence and mechanical vibration, which also affect the phase shift accuracy. Next, we present a brief discussion of these factors.

Piezoelectric transducer (PZT). The most common way to vary the phase difference between two beams in an interferometer is to apply a voltage to a PZT on which the specimen surface is mounted. Unfortunately, PZT suffers two fundamental error when it operates in open-loop control: non-linearity, where PZT displacement is not always a linear function of applied voltage [4, 11–13], and hysteresis, which the PZT displacements during contraction and expansion are different [4, 14]. In this dissertation, we will focus on the effect of PZT nonlinearity in phase measurement.

Atmospheric turbulence. Air current, air temperature, atmospheric pressure, and air humidity alter the refractive index on the optical path [15]. Thus, a length variation of the optical path translates into phase shift error.

Vibration. In practice, if the exposure time to record interferograms is too long and the vibration amplitude is larger than half a wavelength, then the fringes visibility will be destroyed. On the other hand, when the exposure time is much less than the vibration period, vibrations of even a small amplitude will introduce errors in the measured phase [16–21].

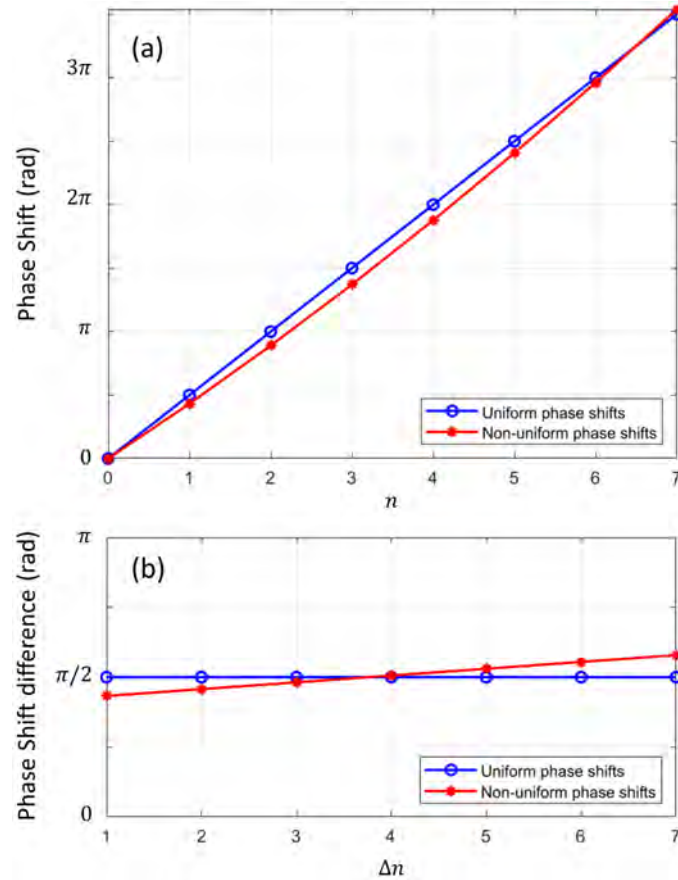


Figure 3.1: Uniform (blue line) and non-uniform (red line) phase-shift distributions. (a) Absolute phase shifts and (b) phase shift differences between two consecutive interferograms.

Taking into account the aforementioned error sources, the actual phase shift is composed by

a nominal value ω_0 and a unknown additional term. So, the mathematical representation for a phase-shifting interferogram, given by Eq. (2.9), should be rewritten as

$$I_n = a + b \cos[\phi + \omega_0 n + \Delta_n], \quad (3.1)$$

where Δ_n represent the phase shift error which has a different value in each phase shift. In this case Δ_n is a band-limited component.

Now, let us define the phase shift function for practical measurement processes

$$\theta_n = \omega_0 n + \Delta_n. \quad (3.2)$$

Here θ_n is given in radians and it is known as *non-uniform phase shift*. This equation means that each amount in phase-shifts corresponds to θ_n instead of $\omega_0 n$; in other words, interferometric data has a different phase step than the expected value. Therefore, Eq. (3.1) can be rewritten as

$$I_n = a + b \cos[\phi + \theta_n], \quad (3.3)$$

Figure 3.1 gives a overview of phase shift distributions. The absolute phase shifts respect to the first interferogram are shown in Fig. 3.1(a), whereas Fig. 3.1(b) shows the phase shift differences between consecutive interferograms. Uniform phase shift and non-uniform phase shifts are drawn in blue line and red line, respectively.

3.2 MATHEMATICAL ANALYSIS

Non-uniform phase shift distribution, given by Eq. (3.2), can be expanded as a polynomial function of the unperturbed phase shift value ω_0 [9, 10], so that

$$\theta_n = \omega_0 n + \kappa_1 n + \kappa_2 n^2 + O(n^3), \quad (3.4)$$

here κ_1 and κ_2 represent the linear and quadratic nonlinearity coefficients of the PZT motion, respectively [11, 24]. These coefficients are small and unknown parameters that can change for each realization. This approach is based on the assumption that the PZT nonlinearity is so small that a quadratic function is sufficient to describe the PZT displacement [11]. Therefore, all terms of order 3 and higher are negligible.

Substituting Eq. (3.4) into Eq. (2.17), we have

$$\frac{\hat{b}}{2} e^{i\hat{\phi}} = a \sum_{n=0}^{N-1} c_n + \frac{b}{2} e^{i\phi} \sum_{n=0}^{N-1} c_n e^{i\theta_n} + \frac{b}{2} e^{-i\phi} \sum_{n=0}^{N-1} c_n e^{-i\theta_n}. \quad (3.5)$$

Now, taking account the first conditions given by Eq. (2.13), $H(0) = 0$, we have

$$a \sum_{n=0}^{N-1} c_n = 0. \quad (3.6)$$

Then, Eq. (3.5) is rewritten as

$$\frac{\hat{b}}{2} e^{i\hat{\phi}} = \frac{b}{2} e^{i\phi} S_1 \left(1 + \frac{S_2}{S_1} e^{-2i\phi} \right), \quad (3.7)$$

where

$$S_1 = \sum_{n=0}^{N-1} c_n e^{i\theta_n}, \quad S_2 = \sum_{n=0}^{N-1} c_n e^{-i\theta_n}. \quad (3.8)$$

Two main conditions are recognized from Eq. (3.7). First, $S_1 = 1$ in order to eliminate the spurious piston in the estimated phase, and second, $S_2 = 0$ in order to suppress the double-frequency ripple distortions in the estimated phase.

By using the Maclaurin series [47], it is possible to achieve the first-order approximations of the following expression: $\exp i(\kappa_1 n + \kappa_2 n^2)$, so that

$$e^{i(\kappa_1 n + \kappa_2 n^2)} \approx 1 + \kappa_1 n + \kappa_2 n^2. \quad (3.9)$$

Then, substituting Eq. (3.9) into Eq. (3.8), we have

$$S_1 \approx \sum_{n=0}^{N-1} c_n e^{in\omega_0} + \kappa_1 \sum_{n=0}^{N-1} (in) c_n e^{in\omega_0} - i\kappa_2 \sum_{n=0}^{N-1} (in)^2 c_n e^{in\omega_0} = 1, \quad (3.10)$$

$$S_2 \approx \sum_{n=0}^{N-1} c_n e^{-in\omega_0} - \kappa_1 \sum_{n=0}^{N-1} (in) c_n e^{-in\omega_0} + \kappa_2 \sum_{n=0}^{N-1} (in)^2 c_n e^{-in\omega_0} = 0. \quad (3.11)$$

Now, let us consider the m -th derivative of $H(\omega)$, which is given by

$$H^{(m)}(\omega) = \sum_{n=0}^{N-1} (in)^m c_n e^{in\omega_0}. \quad (3.12)$$

Thus, Eqs. (3.10) and (3.11) can be rewritten as

$$S_1 = H(\omega_0) + \kappa_1 H'(\omega_0) - i\kappa_2 H''(\omega_0), \quad (3.13)$$

$$S_2 = H(-\omega_0) - \kappa_1 H'(-\omega_0) + i\kappa_2 H''(-\omega_0). \quad (3.14)$$

Therefore, besides the quadrature conditions given in Eq. (2.13), it is necessary to add the

following conditions

$$H'(\omega) \Big|_{\omega=-\omega_0} = 0 \quad H''(\omega) \Big|_{\omega=-\omega_0} = 0 \quad (3.15)$$

in order to suppress the double-frequency ripple distortions, and the following condition

$$H'(\omega) \Big|_{\omega=\omega_0} = 0 \quad H''(\omega) \Big|_{\omega=\omega_0} = 0 \quad (3.16)$$

in order to eliminate the spurious piston. All of these in order to overcome errors derived from the non-uniform phase shifts.

3.3 ENHANCED FOUR-FRAME PSA

FTF conditions established in Eqs. (2.13), (3.15) and (3.16) can be translated into a linear system $\mathbf{A} \mathbf{x} = \mathbf{b}$, where \mathbf{A} is an N -by- N squared matrix, whereas \mathbf{x} and \mathbf{b} are column vectors of size N -by-1.

$$[\mathbf{b}]_n = \delta_{n,1}, \quad \mathbf{x} = \mathbf{A}^{-1} \mathbf{b}, \quad c_n = [\mathbf{x}]_n \quad (3.17)$$

where $\delta_{m,n}$ is the Kronecker delta and the coefficient c_n are given by the elements of the column vector \mathbf{x} .

3.3.1 FOUR-FRAME PSA

Firstly, let us consider the well-known four-frame PSA [2]. This PSA can be described by the following four conditions:

$$\begin{aligned} H(\omega_0) &= 1, & H(0) &= 0, & H(-\omega_0) &= 0, & (3.18) \\ H(2\omega_0) &= 0. \end{aligned}$$

Note that, the first line of Eq. (3.18) are the quadrature conditions given by Eq. (2.13), and the second line, $H(2\omega_0) = 0$, correspond to the condition to reject the second distorting harmonics (see subsection 2.4.2). Then, these four conditions are translated into

$$\begin{aligned} [\mathbf{A}]_{0,n} &= e^{in\omega_0}, & [\mathbf{A}]_{1,n} &= 1, & [\mathbf{A}]_{2,n} &= e^{-in\omega_0}, & (3.19) \\ [\mathbf{A}]_{3,n} &= e^{2in\omega_0}. \end{aligned}$$

For a phase shift of $\omega_0 = \pi/2$, the explicit linear system is given by

$$\begin{pmatrix} 1 & i & -1 & -i \\ 1 & 1 & 1 & 1 \\ 1 & -i & -1 & i \\ 1 & -1 & 1 & -1 \end{pmatrix} \begin{pmatrix} c_0 \\ c_1 \\ c_2 \\ c_3 \end{pmatrix} = \begin{pmatrix} 1 \\ 0 \\ 0 \\ 0 \end{pmatrix}. \quad (3.20)$$

This linear system can be easily solved using a program computer (e.g. Wolfram Mathematica). Thus, we obtain $c_n = (1/4)\{1, -i, -1, i\}$. The analytic signal constructed from this coefficients is

$$\frac{\hat{b}}{2} e^{i\hat{\phi}_{ff}} = I_0 - iI_1 - I_2 + iI_3.$$

This equation has been previously stated in Eq. (2.19), and it is rewritten for readers convenience. The term $(1/4)$ in c_n is a global factor which do not affect the measured phase value. Magnitude and phase of the FTF of this PSA are depicted in Fig. 3.2(a).

3.3.2 SIX-FRAME PSA

Secondly, let us add to the conditions given by the Eq. (3.18), the conditions given by the Eq. (3.15). So, we have

$$\begin{aligned} [\mathbf{A}]_{0,n} &= e^{in\omega_0}, & [\mathbf{A}]_{1,n} &= 1, & [\mathbf{A}]_{2,n} &= e^{-in\omega_0}, \\ [\mathbf{A}]_{3,n} &= e^{2in\omega_0}, & [\mathbf{A}]_{4,n} &= (in)e^{-in\omega_0}, & [\mathbf{A}]_{5,n} &= (in)^2 e^{-in\omega_0}. \end{aligned} \quad (3.21)$$

From Eq. (3.21) and for a phase shift of $\omega_0 = \pi/2$, the explicit linear system is given by

$$\begin{pmatrix} 1 & i & -1 & -i & 1 & i \\ 1 & 1 & 1 & 1 & 1 & 1 \\ 1 & -i & -1 & i & 1 & -i \\ 1 & -1 & 1 & -1 & 1 & -1 \\ 0 & 1 & -2i & -3 & 4i & 5 \\ 0 & i & 4 & -9i & -16 & 25 \end{pmatrix} \begin{pmatrix} c_0 \\ c_1 \\ c_2 \\ c_3 \\ c_4 \\ c_5 \end{pmatrix} = \begin{pmatrix} 1 \\ 0 \\ 0 \\ 0 \\ 0 \\ 0 \end{pmatrix}. \quad (3.22)$$

Solving this linear system, we obtain $c_n = (1/16)\{1, -3i, -4, -4i, 3, -i\}$. Then, its analytic signal is given by

$$\frac{\hat{b}}{2}e^{i\hat{\phi}_{sf}} = I_0 - 3iI_1 - 4I_2 - 4iI_3 + 3I_4 - iI_5. \quad (3.23)$$

This PSA was reported, but in a different way, by Schmit and Creath [5].

Magnitude and phase of the FTF of six-frame PSA are depicted in Fig. 3.2(b). Note that $|H(\omega)| \approx 0$ around $\omega = -\omega_0$, it is highlighted in the stripped area. This is the main condition to suppress the double-frequency ripple distortions [43], phase error due to linear detuning ($\kappa_1 n$) and quadratic detuning ($\kappa_2 n^2$).

3.3.3 EIGHT-FRAME PSA

Lastly, let us join the conditions given by Eq. (3.18), (3.15), and (3.16), so that

$$\begin{aligned} [\mathbf{A}]_{0,n} &= e^{in\omega_0}, & [\mathbf{A}]_{1,n} &= 1, & [\mathbf{A}]_{2,n} &= e^{-in\omega_0}, \\ [\mathbf{A}]_{3,n} &= e^{2in\omega_0}, & [\mathbf{A}]_{4,n} &= (in)e^{-in\omega_0}, & [\mathbf{A}]_{5,n} &= (in)^2 e^{-in\omega_0}, \\ [\mathbf{A}]_{6,n} &= (in)e^{in\omega_0}, & [\mathbf{A}]_{7,n} &= (in)^2 e^{in\omega_0}. \end{aligned} \quad (3.24)$$

In other words, for a phase shift of $\omega = \pi/2$:

$$\begin{pmatrix} 1 & i & -1 & -i & 1 & i & -1 & -i \\ 1 & 1 & 1 & 1 & 1 & 1 & 1 & 1 \\ 1 & -i & -1 & i & 1 & -i & -1 & i \\ 1 & -1 & 1 & -1 & 1 & -1 & 1 & -1 \\ 0 & 1 & -2i & -3 & 4i & 5 & 6i & -7 \\ 0 & i & 4 & -9i & -16 & 25i & 36 & -49i \\ 0 & -1 & -2i & 3 & 4i & -5 & -6i & 7 \\ 0 & -i & 4 & 9i & -16 & -25i & 36 & 49i \end{pmatrix} \begin{pmatrix} c_0 \\ c_1 \\ c_2 \\ c_3 \\ c_4 \\ c_5 \\ c_6 \\ c_7 \end{pmatrix} = \begin{pmatrix} 1 \\ 0 \\ 0 \\ 0 \\ 0 \\ 0 \\ 0 \\ 0 \end{pmatrix}. \quad (3.25)$$

Solving this linear system, we have $c_n = (1/32)\{14, -23i, -6, i, -6, 15i, -2, 7i\}$. Then, its analytic signal is given by

$$\frac{\hat{b}}{2}e^{i\hat{\phi}_{sf}} = 14I_0 - 23iI_1 - 6I_2 + iI_3 - 6I_4 + 15iI_5 - 2I_6 + 7iI_7. \quad (3.26)$$

The eight-frame PSA is a novel contribution which was reported by us in [48]. Magnitude and phase of the FTF of this PSA are depicted in Fig. 3.2(c). In this case, besides of $|H(\omega)| \approx 0$ in the vicinity of $\omega = -\omega_0$, now the phase of the FTF is zero around $\omega = \omega_0$, they are highlighted in the striped area. These two outstanding features are the condition to suppress the double-frequency ripple distortions and to eliminate the spurious piston in phase measurement.

Figure 3.2 illustrate the evolution of the four-frame PSA in order to suppress the double-frequency ripple distortion (six-frame PSA) and, then, to eliminate the spurious piston (eight-frame PSA).

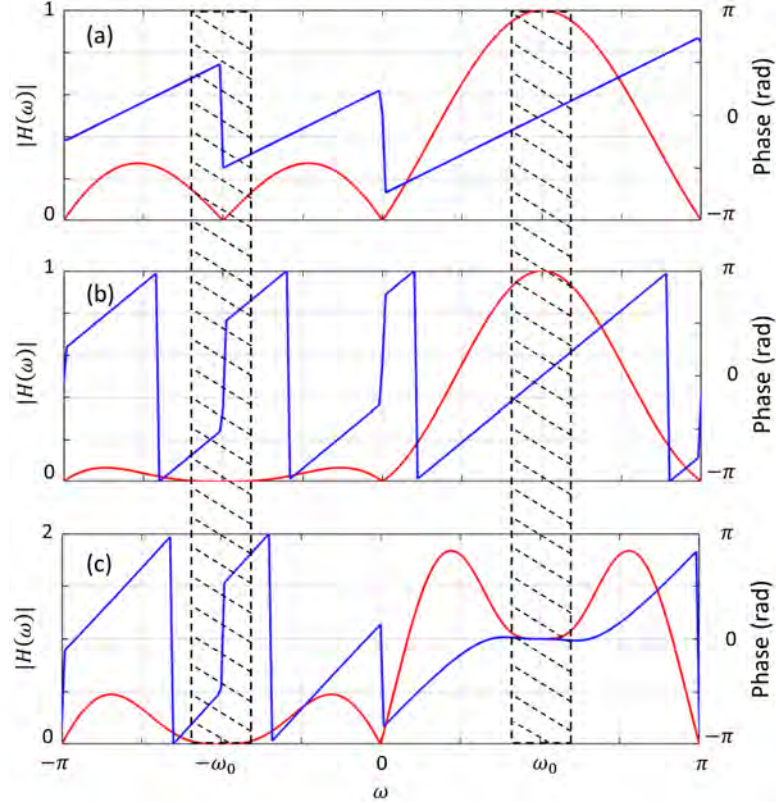


Figure 3.2: Magnitude (red line) and phase (blue line) of the FTF of (a) four-frame PSA, (b) six-frame PSA, and (c) eight-frame PSA.

Roots of the characteristic polynomials of the four-frame PSA, six-frame PSA, and eight-frame PSA are shown in Fig. 3.3(a), 3.3(b) and 3.3(c), respectively. Multiple roots are denoted by a blue dot surrounded by circles (See appendix A). Four-frame PSA has single roots at $z = \{1, -1, -i\}$. Whereas, regarding to four-frame PSA, six-frame PSA has two additional roots at $z = -i$ because of that this PSA is insensitivity against phase shift terms associated to linear detuning ($\kappa_1 n$) and quadratic detuning ($\kappa_2 n^2$). On the other hand, regarding to six-frame PSA, eight-frame PSA has two exceptional roots at $z = \{-0.3977 + 1.3571i, 0.3977 + 1.3571i\}$. Due to this roots along the complex unitary circle, this PSA is capable to eliminate the spurious piston.

Table 3.1 resumes the main features of the three studied PSAs. It indicates number of frames

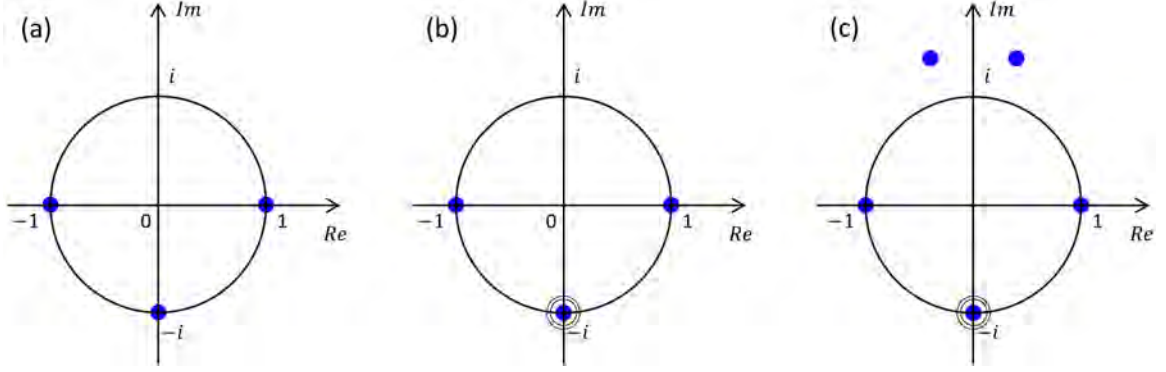


Figure 3.3: Roots position of (a) four-frame PSA, (b) six-frame PSA, and (c) eight-frame PSA.

(N), phase shift value (ω_0), PSA coefficients (c_n), harmonics rejection capabilities, and signal-to-noise ratio gain (G_{SNR}).

Table 3.1: Figures of merits for four-frame PSA, six-frame PSA, and eight-frame PSA.

PSA	N	ω_0	Coefficient c_n	Harmonics*	G_{SNR}
four-frame	4	$\pi/2$	$\frac{1}{4}\{1, -i, -1, i\}$	$-7, -3, 5, 9$	4
six-frame	6	$\pi/2$	$\frac{1}{16}\{1, -3i, -4, 4i, 3, -i\}$	$-7, -3, 5, 9$	4.92
eight-frame	8	$\pi/2$	$\frac{1}{32}\{14, -23i, -6, i, -6, 15i, -2, 7i\}$	$-7, -3, 5, 9$	0.95

* It refers to non-rejected distorting harmonics within the normalized frequency range $\omega/\omega_0 = [-10, 10]$.

3.4 SIMULATION RESULTS

Numerical simulations are performed in order to validate the previous mathematical analysis. Thus, an interferogram set composed by eight fringe patterns ($N = 8$) was generated, each interferogram has a size of 512×512 pixels. Background illumination and local contrast function are constants, whereas the phase map $\varphi(x, y)$ is given by

$$\varphi(x, y) = 10\pi e^{-\left(\frac{x^2+y^2}{10^5}\right)}. \quad (3.27)$$

On the other hand, phase shifts are ruled by Eq. (3.4), where $\omega_0 = \pi/2$, $\kappa_1 = -0.25$, and $\kappa_2 = 0.0383$. These values describe the non-uniform phase shift distribution shown in Fig. 3.1(a). In this case, the maximum deviation from the nominal phase shift is 0.2479 rad ($\approx 14^\circ$), it can be seen from Fig. 3.1(b).

Two types of simulations are carried out. First, phases are computed from noiseless interferograms, and second, phases are computed from interferograms corrupted by AWGN with $\sigma = 3$. Figure 3.4 shows simulated noiseless interferograms and Figure 3.5 shows computed phases by using four-frame PSA, six-frame PSA, and eight-frame PSA.

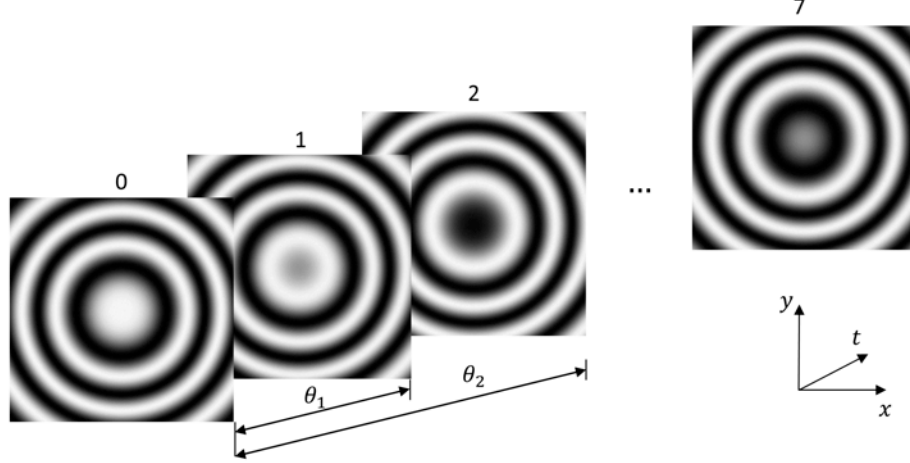


Figure 3.4: Eight simulated interferograms used as input data for phase demodulation.

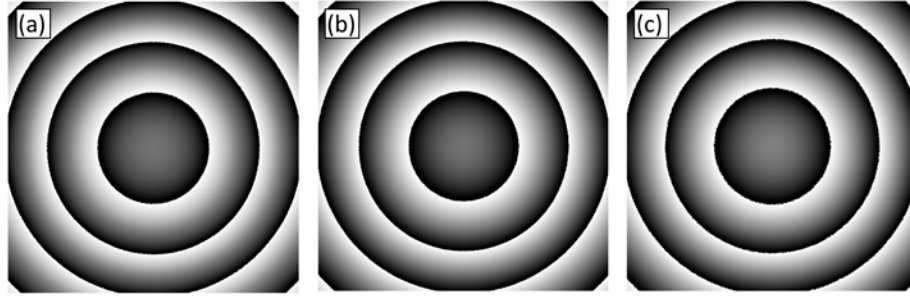


Figure 3.5: Phase map measured by using (a) four-frame PSA, (b) six-frame PSA, and (c) eight-frame PSA.

In order to compare the performance of the three referred PSAs, we use the height error parameter. But before, let us define the 1-D phase error parameter

$$\varphi_{error}(x) = \varphi(x) - \hat{\varphi}(x). \quad (3.28)$$

Here $\varphi(x)$ is the nominal phase value governed by Eq. (3.27), and $\hat{\varphi}(x)$ is the estimated phase. Phase error and height error are proportional, as stated in Eq. (2.26).

Height profile errors computed from noiseless interferograms are shown in Fig. 3.6(a). From this graphic, three main features are distinguished: 1) height error computed from four-frame PSA exhibit a double-frequency ripple distortion and a spurious piston. 2) height error computed from six-frame PSA do not exhibit a double-frequency ripple distortion but it present a spurious piston equal to 16.7077 nm. 3) height error computed from eight-frame PSA is error free. These results prove us right. Similar behavior is observed in Fig. 3.6(b), but in this case, height errors are corrupted by noise.

Table 3.2 details the root-mean-square (*rms*) and the peak-to-valley (*p-v*) errors, these parameters were computed from height profile errors, shown in Fig. 3.6. Note that in both cases, noiseless and noisy interferograms, the *p-v* error and the *rms* error corresponding to four-frame PSA

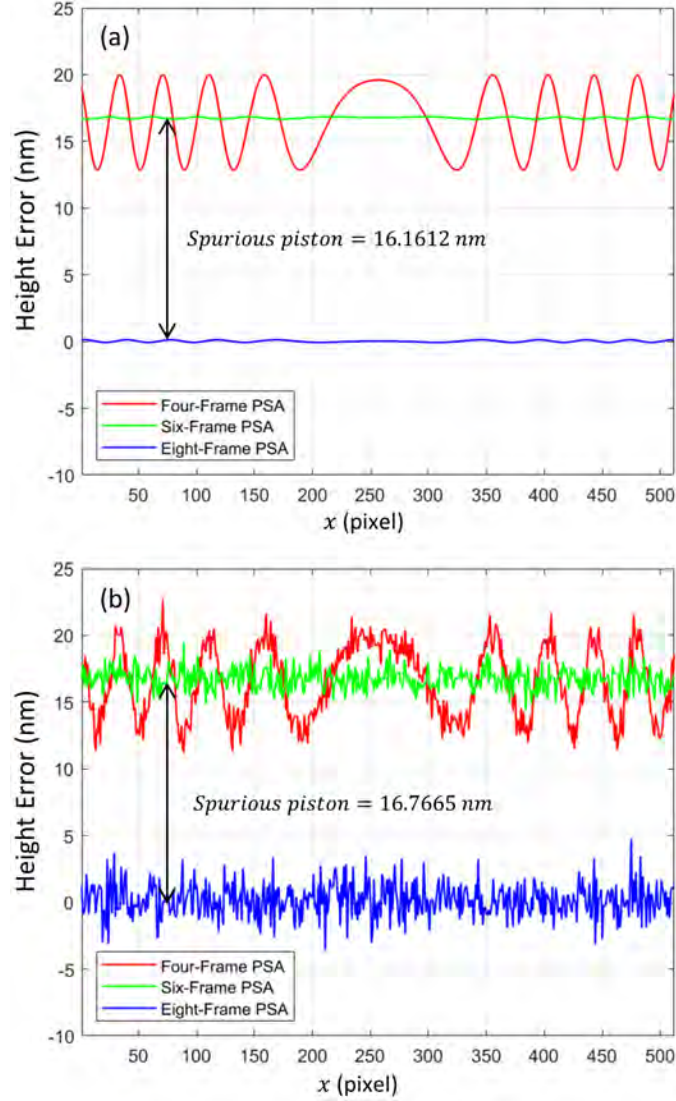


Figure 3.6: Phase errors computed from (a) noiseless interferograms and (b) interferograms corrupted by AWGN with $\sigma = 3$.

and six-frame PSA, respectively, are not negligible. Thus, in real measurement (considering a wavelength of 660 nm), these errors can be misinterpreted as real physical quantities, in one case as a surface with sinusoidal variation, and in other case as additional thickness of ≈ 16 nm.

3.5 DISCUSSIONS

We use the four-frame PSA to illustrate that this algorithm can neither suppress the double-frequency ripple distortion nor eliminate the spurious piston. But, if we add to it conditions given by Eq. (3.15), this modified PSA is capable to suppress the double-frequency ripple distortion, after that, if we add again those condition given by Eq. (3.16), this new PSA is capable

Table 3.2: Computed root-mean-square (rms) errors and peak-to-valley ($p-v$) errors by the four-frame PSA, six-frame, and eight-frame PSA.

PSA	Noiseless interferograms		Noisy interferograms	
	rms (nm)	$p-v$ (nm)	rms (nm)	$p-v$ (nm)
four-frame	16.7077	7.1329	16.7463	11.5200
six-frame	16.7612	0.1780	16.7665	5.1581
eight-frame	0.1040	0.1968	1.2681	8.3274

to remove both the double-frequency ripple distortion and the spurious piston. In each process, two frames are added to the analytic signal in order to measure the phase.

Process to modify the four-frame PSA, in order to avoid errors in phase measurement, are labeled as evolution of the four-frame PSA, this is illustrated in Fig. 3.2. Here, on the left side, $|H(\omega)|$ goes from being 0 at $\omega = -\omega_0$ in Fig. 3.2(a) to being 0 around $\omega = -\omega_0$ in Fig. 3.2(c), whereas on the right side, FTF phase goes from being 0 at $\omega = \omega_0$ in Fig. 3.2(a) to being 0 around $\omega = \omega_0$ in Fig. 3.2(c), all of it is remarked in the stripped area.

In a similar way, as it was proceeded for the four-frame PSA, most conventional error-correcting PSAs can be modified in order to avoid errors in phase measurement, some examples was reported by us in Ref. [48].

Moreover, readers should note that it is straightforward to generalize this procedure for high-order of non-linearity, e.g. $\kappa_3 n^3$ in Eq. (3.4). In this case, we would need to use the following conditions

$$H'''(\omega) \Big|_{\omega=-\omega_0} = 0 \quad \text{and} \quad H'''(\omega) \Big|_{\omega=\omega_0} = 0. \quad (3.29)$$

Nonetheless, this is not a good idea because the sensitivity to random noise increases significantly with each additional spectral condition.

4

Surface topography of aluminum thin film

In this chapter, we describe a specific procedure to measure the phase from a set of non-uniform phase-shifting interferograms, these interferograms are acquired from a Michelson interferential microscope and they are used to estimate the surface topography of an aluminum thin film. This procedure starts measuring the phase shift between interferograms by using the Fourier method. Then, the phase shifts, specifically phase shift errors, are used to define the modified phase-shifting interferogram. This modified data is used to design a suitable PSA in order to suppress the double-frequency ripple distortion, to do this we use the FTF conditions established in previous chapter. In this specific application, the spurious piston error is irrelevant because there is a reference surface to measure the height distribution. Lastly, we present a 3-D map of the aluminum thin film surface, which is compared with other methods like Fourier method, principal component analysis, and least-square PSA.

4.1 GROUNDWORK

Nine experimental interferograms ($N = 9$) acquired from the Michelson interferential microscope are shown in Fig. 4.1, each interferogram has a size of 1024×1280 pixels. Phase shifts among these interferograms are non-uniform because a PZT operating in open-loop is used as phase shifter. Consequently, actual phase shift is composed by a nominal value $\omega_0 n$ and a phase

shift error Δ_n , and phase shifts are governed by Eq. (3.1), as it was stated in previous Chapter.

By means of previous measurements, we figure out that a voltage step equal to 1.8 V produced phase shifts around $\omega_0 = \pi/2$ [49]. So, phase shifts are generated by applying this voltage step over the PZT. Keep in mind that an aluminum thin film, the specimen surface, is coupled to the PZT (see Fig. 2.2).

Specimen surface is composed by a aluminum layer deposited over a silicon substrate. Height distribution of the thin film is measured using the substrate surface as reference, consequently, the spurious piston is no relevant in this specific application. Thin film surface can be distinguished from Fig. 4.1 as the brightest area, the rest is the substrate surface.

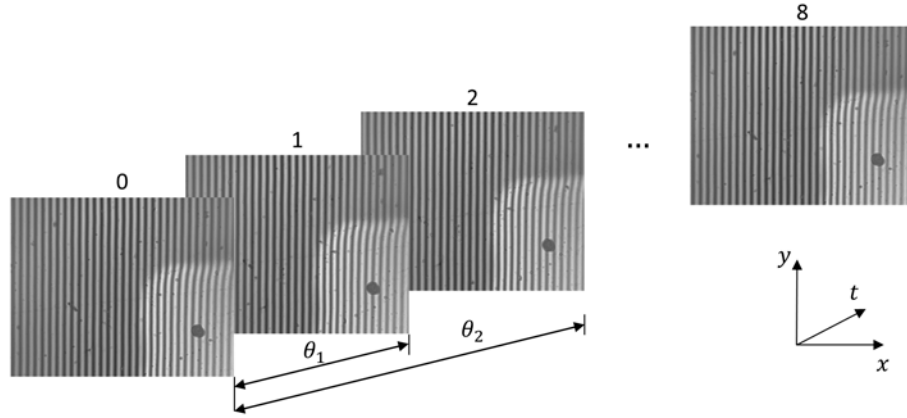


Figure 4.1: Nine ($N = 9$) phase shifting interferogram acquire from Michelson interferential microscope. Information of the aluminum thin film is encoded into the interferometric fringes.

In this chapter, in some cases, the spatial dependency (x, y) is considered because a spatial method will be used to measure the phase shift distribution. All these mentioned ideas will help to understand the following sections.

4.2 PHASE SHIFTS MEASUREMENT

In order to measure the phase shift among the interferograms, we employ the Fourier transform method [50, 51]. Thus, let us start by taking the spatial Fourier transform of the non-uniform phase shifting interferogram $I_n(x, y)$, so that

$$I_n(u, v) = A(u, v) + e^{i\theta_n} C(u - u_0, v) + e^{-i\theta_n} C(u + u_0, v). \quad (4.1)$$

Where

$$A(u, v) = \mathcal{F}\{a(x, y)\} \quad \text{and} \quad C(u, v) = \mathcal{F}\left\{\frac{1}{2}b(x, y)e^{i[\phi(x, y) + \theta_n]}\right\}.$$

Equation (4.1) is computed under the assumption that the spatial variation of $a(x, y)$, $b(x, y)$, and $\phi(x, y)$ are slow compared with the spatial carrier u_0 . This Fourier spectrum is split into three lobes, two lateral lobes located at $u = \{-u_0, u_0\}$ and the main lobe located at $u = 0$. Here, it is crucial that the main-lobe and the lateral-lobes do not overlap, it implies to use interferograms with high fringe density, as shown in Fig. 4.1. Fringe density can be easily increased by tilting the reference mirror in Fig. 2.1, in other words, by increasing the value of α .

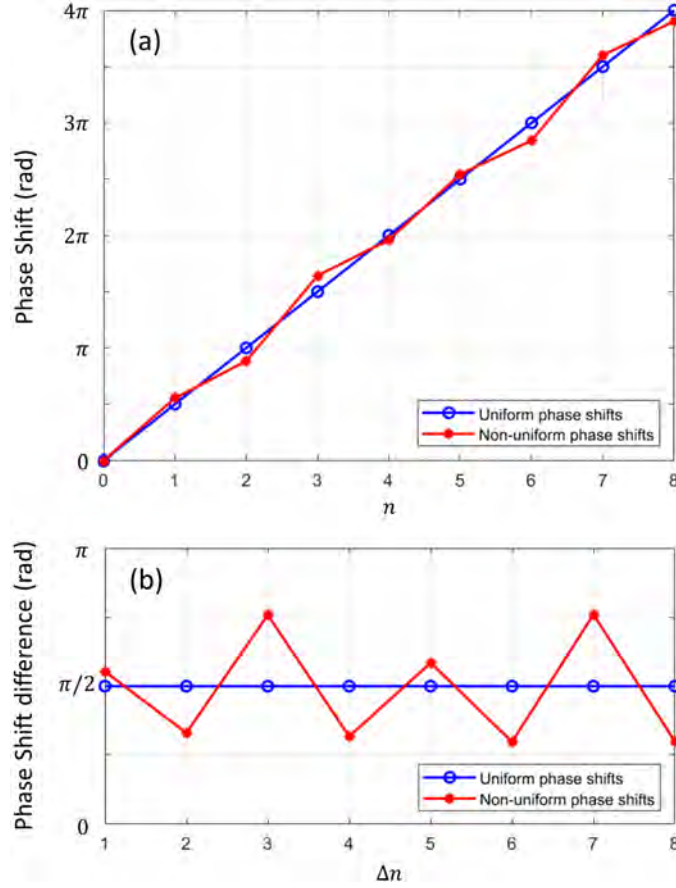


Figure 4.2: Uniform (blue line) and non-uniform (red line) phase-shift distributions. (a) Sequential phase shifts and (b) phase-shift differences among consecutive interferograms.

Then, we use a band pass filter centered at $u = u_0$ in order to isolate one side-lobe of the spectrum [43, 50, 52]. After that, the inverse Fourier transform is applied and it results in

$$z_n(x, y) = \frac{1}{2} b(x, y) e^{i[\phi(x, y) + \theta_n]}. \quad (4.2)$$

This procedure is repeated for each interferogram. Thus, the sequential phase shift can be estimated as

$$\theta_n - \theta_0 = \text{mode}\{\arg[z_n(x, y)z_0^*(x, y)]\}. \quad (4.3)$$

Here $\theta_0 = 0$, it is the initial condition, and mode is the statistics parameters which gives the value that appears most often over the whole matrix (x, y) .

Figure 4.2(a) shows in red the measured phase shifts by using Eq. (4.3), note that these phase shifts are measured with respect to the first interferogram. In the same way, it is possible measuring the phase difference between two consecutive interferograms by doing $\theta_{n+1} - \theta_n$, this result is shown in Fig. 4.2(b). In both cases, the ideal phase shift is drawn in blue, in one case, there is a linear dependency between image number and the phase shift, and in other case, the phase shift differences are constant.

In this dissertation, we consider the Fourier method to estimate the phase shifts because it is robust, it use a whole matrix to estimate a single value. However, there are other methods to determine the phase shifts, such as the sine-fitting method [53], the cross-correlation method [54], and the Lissajous elliptic fitting algorithm [55]. On the other hand, in the absence of spatial carrier (u_0), we can use the Fourier–Hilbert transform proposed by Larkin [56].

Readers should note that this procedure was made considering a single spatial carrier in the x direction. Nonetheless, this procedure can be expanded for spatial carriers with non-zero component in the y direction.

4.3 MODIFIED PHASE SHIFTING INTERFEROGRAM

Let us define the modified phase-shifting interferogram, which is given by the following expression

$$J_n = I_n e^{-i\Delta_n}. \quad (4.4)$$

Here, Δ_n is the phase shift error, studied in section 3.1. This parameter can be easily estimated by using Eq. (3.2), keep in mind that the phase shift distribution θ_n has been already determined in previous section, and that the nominal value of the phase shift is $\omega_0 = \pi/2$.

Now, rewritten I_n and J_n using the Euler's formula, we have

$$I_n = a + \frac{b}{2} e^{i[\phi + \omega_0 n + \Delta_n]} + \frac{b}{2} e^{-i[\phi + \omega_0 n + \Delta_n]}, \quad (4.5)$$

$$J_n = a e^{-i\Delta_n} + \frac{b}{2} e^{i[\phi + \omega_0 n]} + \frac{b}{2} e^{-i[\phi + \omega_0 n + 2\Delta_n]}. \quad (4.6)$$

Then, computing the discrete Fourier transform of Eqs. (4.5) and (4.6), we have

$$I(\omega) = a\delta(\omega) + \frac{b}{2} e^{i\phi} D(\omega - \omega_0) + \frac{b}{2} e^{-i\phi} D^*(\omega + \omega_0), \quad (4.7)$$

$$J(\omega) = aD(\omega) + \frac{b}{2}e^{i\varphi}\delta(\omega - \omega_0) + \frac{b}{4}e^{-i\varphi}D^*\left(\frac{\omega + \omega_0}{2}\right), \quad (4.8)$$

where $D(\omega) = \mathcal{F}\{\exp[i\Delta(t)]\}$.

Figure 4.3(a) shows schematically the spectrum of non-uniform phase-shifting interferograms $I(\omega)$, here, note that there are lobes located at $\omega = \{-\omega_0, \omega_0\}$ instead of Dirac delta functions, which is usual in interferograms with uniform phase shift (see Fig. 2.5).

On the other hand, Fig. 4.3(b) shows the spectrum of the modified phase-shifting interferogram. Here, there is a Dirac delta function at $\omega = \omega_0$, and the bandwidth of the lobe located at $\omega = -\omega_0$ is increased. At this stage, all of it is our main goal in order to design a suitable PSA.

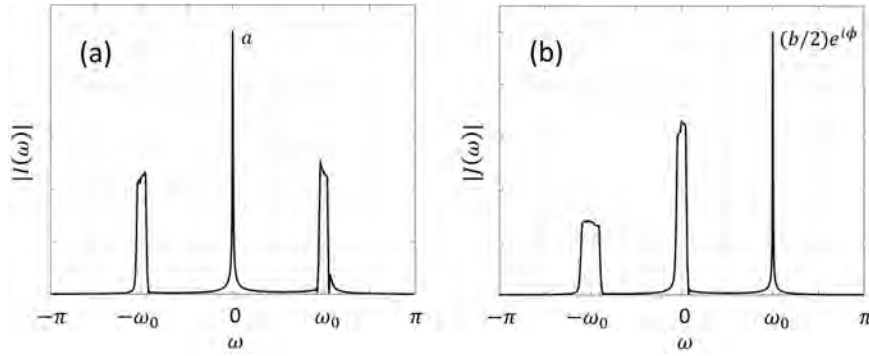


Figure 4.3: Spectrum of (a) non-uniform and (b) modified phase shifting interferogram.

4.4 A CUSTOM-MADE NINE-FRAME PSA

Now, taking account the spectrum of the modified phase shifting interferogram $J(\omega)$, given by Eq. (4.8) and depicted in Fig. 4.3, and in order to measure the searched phase, we propose a PSA with the following condition: first, a third-order zero at $\omega = -\omega_0$, so that

$$H'(\omega)\Big|_{\omega=-\pi/2} = 0, \quad H''(\omega)\Big|_{\omega=-\pi/2} = 0, \quad H'''(\omega)\Big|_{\omega=-\pi/2} = 0, \quad (4.9)$$

and second, one additional zero at $\omega = \{0, \pi\}$ is added, so that

$$H'(\omega)\Big|_{\omega=0} = 0, \quad H'(\omega)\Big|_{\omega=\pi} = 0. \quad (4.10)$$

Conditions stated by Eqs. (4.9), and (4.10) are additional to those given by Eq. (3.18). These last conditions are useful to flatten $|H(\omega)|$ at $\omega = \{-\pi, -\pi/2, 0\}$. All of it in order to obtain high-quality phase estimation.

Then, conditions given in Eqs. (3.18), (4.9), and (4.10) are translated into

$$\begin{aligned}
[\mathbf{A}]_{0,n} &= e^{in\omega_0}, & [\mathbf{A}]_{1,n} &= 1, & [\mathbf{A}]_{2,n} &= in, \\
[\mathbf{A}]_{3,n} &= e^{-in\omega_0}, & [\mathbf{A}]_{4,n} &= (in)e^{-in\omega_0}, & [\mathbf{A}]_{5,n} &= (-n^2)e^{-in\omega_0}, \\
[\mathbf{A}]_{6,n} &= (-in^3)e^{-in\omega_0}, & [\mathbf{A}]_{7,n} &= e^{2in\omega_0}, & [\mathbf{A}]_{8,n} &= (in)e^{2in\omega_0}.
\end{aligned} \tag{4.11}$$

Then, proceeding in the same way, as in section 3.3, we obtain $c_n = (1/64)\{1, -4i, -8, 12i, 14, -12i, -8, 4i, 1\}$. And, its analytic signal is given by

$$\frac{\hat{b}}{2} e^{i\hat{\phi}_{nf}} = I_0 - 4iI_1 - 8I_2 + 12iI_3 + 14I_4 - 12iI_5 - 8I_6 + 4iI_7 + I_8. \tag{4.12}$$

The spectrum of the modified non-uniform phase-shifting interferogram $J(\omega)$ superposed by the FTF magnitude of nine-frame PSA are depicted in Fig. 4.4(a), here, note that $|H(\omega)|$ has the precise conditions to remove those lobes located at $\omega = \{-\omega_0, 0\}$.

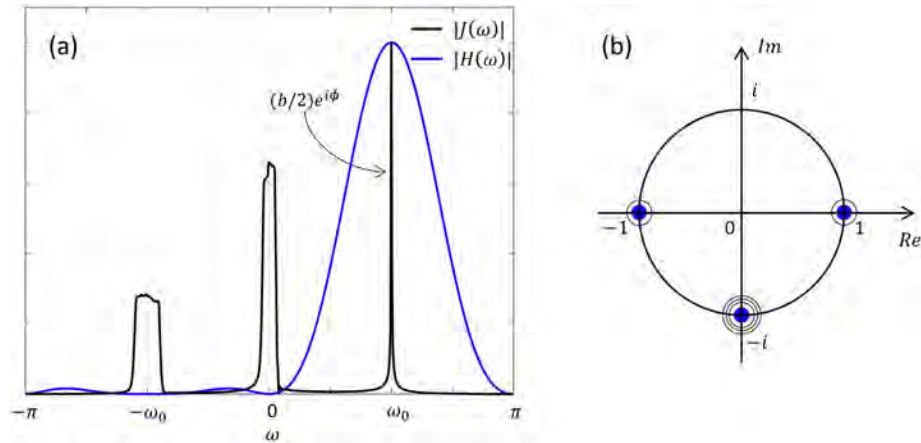


Figure 4.4: (a) Spectrum of the modified non-uniform phase-shifting interferogram (black line) superposed by the FTF magnitude of nine-frame PSA (blue line). (b) Root positions of its corresponding characteristic polynomial.

Figure 4.4(b) shows the root position of nine-frame PSA, which was calculated using the characteristic polynomial of PSA (see appendix A), this PSA has double roots at $z = \{1, -1\}$ and four roots at $z = -i$.

Figures of merit of this nine-frame PSA like signal-to-noise ratio gain G_{SNR} and harmonic rejection are resumed in Table 4.1.

4.5 EXPERIMENTAL RESULTS

In this section, surface topography of the aluminum thin film is computed. First of all, the searched phase is estimated by using the custom-made nine-frame PSA. In the same way and

Table 4.1: Figures of merits for the proposed nine-frame PSA.

PSA	N	ω_0	Coefficient c_n	Harmonics*	G_{SNR}
nine-frame	9	$\pi/2$	$\frac{1}{64}\{1, -4i, -8, 12i, 14, -12i, -8, 4i, 1\}$	$-7, -3, 5, 9$	6.34

* It refers to non-rejected distorting harmonics within the normalized frequency range $\omega/\omega_0 = [-10, 10]$.

in order to compare the obtained result by using the proposed PSA, we used other three methods for phase measurement like the Fourier Method [50], eight-step frequency-shifted LS-PSA [57], and PCA method [27–30].

Computed phases are defined within $[-\pi, \pi]$, as it was mentioned in Chapter 2. So, a phase unwrapping algorithm is used in order to pass the searched phase $\phi(x, y)$ modulo 2π to a continuous map (see Appendix B).

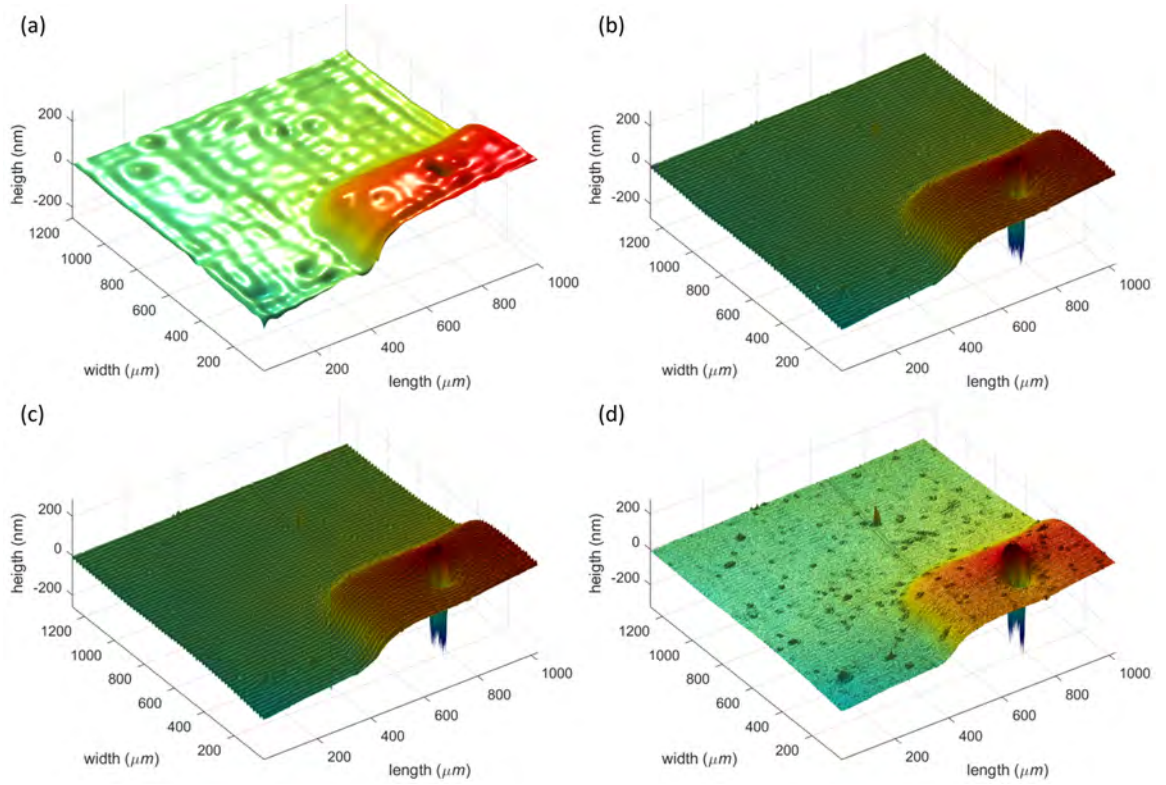


Figure 4.5: Height map using (a) Fourier method, (b) eight-step frequency-shifted LS-PSA, (c) PCA method, and (d) proposed algorithm.

Topographic surfaces of an aluminum thin film by using four different methods are shown in Fig. 4.5. 3-D Surfaces shows the aluminum layer deposited over the silicon substrate, these surfaces permits us to analyze the roughness parameters, thickness, and singularities of the test surface.

In order to illustrate the good performance of the proposed nine-frame PSA, vertical slices of

the height variations are shown in Fig. 4.6. From this figure, specifically the zoomed-in detail area, we distinguish three different results:

First, profile corresponding to Fourier method (red line) is over smoothed, and it is not useful for roughness inspection. This method was used to make visible the main advantage of a PSA over a spatial method in phase demodulation.

Second, profiles corresponding to eight-step LS-PSA (black line) and the PCA method (blue line) exhibit the studied double-frequency ripple distortion, this common error generated by non-uniform phase shift can be misinterpreted as surface shape. Thus, in this specific application, these methods are not useful.

Third, in contrast to other methods, the result obtained by the proposed nine-frame PSA (green line) is free of ripples distortions. This means that the proposed nine-frame PSA has an excellent error-correcting ability for the double-frequency ripple distortion error. So, a good estimation of the surface topography of an aluminum thin film is obtained.

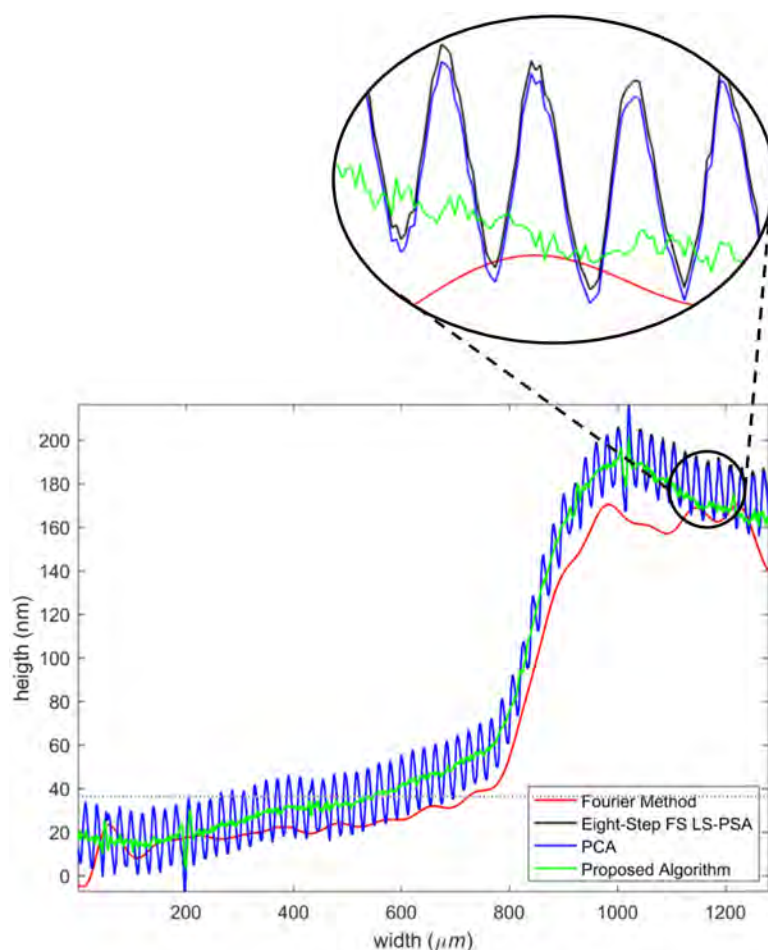


Figure 4.6: Vertical slices of the estimated surfaces using Fourier method (red line), eight-step frequency-shifted LS-PSA (black line), PCA method (blue line), and proposed algorithm (green line).

5

Surfaces with vertical super-resolution

First of all, we would like to point out that when we say vertical super-resolution, we are talking about vertical sensitivity, and it refers to resolve with more details the height variation over the specimen surface by using a synthetic ultraviolet wavelength.

In this chapter, surfaces topography of aluminum thin film with vertical super-resolution are estimated. For this purpose, we use phase shifting interferometry with multiple wavelength. Multiple wavelength in PSI has been widely used for pixel-wise unwrapping via phase differences. Here, we propose to perform phase sums to increase the vertical sensitivity. Thus, several sets of non-uniform phase shifting interferograms were recorded at two different wavelengths, $\lambda_1 = 660$ nm and $\lambda_2 = 530$ nm. Then, estimated phases from each set of interferograms are summed in order to obtain a phase with ultraviolet sensitivity, this phase-sum translated into surfaces topography can be interpreted as if the specimen surface was measured using a light source with ultraviolet wavelength. Finally, we discuss some factors which also alter the super-resolution in PSI.

5.1 MULTIPLE WAVELENGTH IN PSI

The phase measurement procedure in PSI using a single-wavelength can be expanded to two-wavelength [12, 58–61]. Thus, two phase measurements are performed at two different wave-

lengths (λ_1 and λ_2). Then, we have two analytic signals

$$\frac{\hat{b}_1}{2} e^{i\hat{\phi}_1} = \sum_{n=0}^{N-1} c_n \{I_n\}_{\lambda_1}, \quad (5.1)$$

$$\frac{\hat{b}_2}{2} e^{i\hat{\phi}_2} = \sum_{n=0}^{N-1} c_n \{I_n\}_{\lambda_2}. \quad (5.2)$$

Here, $\hat{\phi}_k$ and $\{I_n\}_{\lambda_k}$ represent the estimated phase and a set of phase shifting interferograms, respectively, using λ_k , where $k = 1, 2$.

By multiplying Eq. (5.1) by the complex conjugate of Eq. (5.2), we have

$$\frac{\hat{b}_1}{2} e^{i\hat{\phi}_1} \left[\frac{\hat{b}_2}{2} e^{i\hat{\phi}_2} \right]^* = \frac{\hat{b}_1 \hat{b}_2}{4} e^{i(\hat{\phi}_1 - \hat{\phi}_2)}. \quad (5.3)$$

Then, computing the argument of the right side of Eq. (5.3) and using the relationship between phase and height, given by Eq. (2.26). We have

$$\begin{aligned} \hat{\phi}_1 - \hat{\phi}_2 &= \frac{4\pi}{\lambda_1} W - \frac{4\pi}{\lambda_2} W \\ \hat{\phi}_D &= \frac{4\pi}{\lambda_D} W, \end{aligned} \quad (5.4)$$

where

$$\lambda_D = \frac{\lambda_1 \lambda_2}{|\lambda_1 - \lambda_2|}, \quad (5.5)$$

and it represents the equivalent wavelength for phase-difference [58]. Note that $\lambda_D \gg \{\lambda_1, \lambda_2\}$. So, if λ_1 and λ_2 are in the visible region, λ_D is in the infrared region of the electromagnetic spectrum.

The result given by Eq. (5.4) is an estimated phase-difference $\hat{\phi}_D$ as if the surface W was tested using an infrared wavelength λ_D . Thus, by using two estimated phases at two different wavelengths, we are able to extend the dynamic range of the measurement [12]. Moreover, due to $\lambda_D \gg \{\lambda_1, \lambda_2\}$, the computed phase is not wrapped.

On the other hand, by multiplying Eq. (5.1) by Eq. (5.2), we have

$$\frac{\hat{b}_1}{2} e^{i\hat{\phi}_1} \frac{\hat{b}_2}{2} e^{i\hat{\phi}_2} = \frac{\hat{b}_1 \hat{b}_2}{4} e^{i(\hat{\phi}_1 + \hat{\phi}_2)}. \quad (5.6)$$

Then, by computing the argument of the right side of Eq. (5.6), we have

$$\begin{aligned}\hat{\phi}_1 + \hat{\phi}_2 &= \frac{4\pi}{\lambda_1} W + \frac{4\pi}{\lambda_2} W \\ \hat{\phi}_S &= \frac{4\pi}{\lambda_S} W,\end{aligned}\tag{5.7}$$

where

$$\lambda_S = \frac{\lambda_1 \lambda_2}{\lambda_1 + \lambda_2}.\tag{5.8}$$

In this case $\lambda_S \ll \{\lambda_1, \lambda_2\}$. Consequently, if λ_1 and λ_2 are in the visible region, λ_S is in the ultraviolet region of the electromagnetic spectrum. Thus, the estimated phase-sum $\hat{\phi}_S$ has ultraviolet phase sensitivity and it is highly wrapped. This is known as super-resolution PSI, which is defined as if the estimated phase $\hat{\phi}_S$ was measured using a light source with ultraviolet wavelength [62, 63].

Readers should notice that phase-sum procedure, given by Eq. (5.7), can be expanded to the sum of three or M measured phases. Considering that these phase measurements are performed at unique wavelength λ_1 , we have

$$\begin{aligned}\hat{\phi}_1 + \hat{\phi}_2 + \dots + \hat{\phi}_M &= \frac{4\pi}{\lambda_1} W + \frac{4\pi}{\lambda_1} W + \dots + \frac{4\pi}{\lambda_1} W \\ \hat{\phi}_{SM} &= \frac{4\pi}{\lambda_{SM}} W,\end{aligned}\tag{5.9}$$

where

$$\lambda_{SM} = \frac{\lambda_1}{M}.\tag{5.10}$$

Here, $\hat{\phi}_{SM}$ has far-ultraviolet sensitivity. Therefore, the sensitivity of the phase-sum can be extended from ultraviolet to far-ultraviolet by increasing the number M of demodulated phases.

5.2 GROUNDWORK

Three sets of nine ($N = 9$) non-uniform phase shifting interferograms at $\lambda_1 = 660$ nm, over the same specimen surface but at different measurements, were acquired from the Michelson interferential microscope. Each interferograms have a size of 1024×1280 pixels. In all sets of interferograms, the phase shifts among interferograms are governed by Eq. (3.4). Taking account that the spurious piston is not relevant in this specific application, we use the nine-frame PSA to demodulate the optics phase.

In this dissertation work, we use phase-sum $\hat{\phi}_S$ rather than phase-difference $\hat{\phi}_D$ because, as we stated in previous section, the phase-sum of three demodulated phase has far-ultraviolet sensitivity. Thus, by using a phase-sum $\hat{\phi}_S$ we obtain surfaces topography of an aluminum thin film with vertical super-resolution.

In similar way, a second measurement was carried out, in this case, two sets of nine ($N = 9$) non-uniform phase-shifting interferograms at $\lambda_1 = 660$ nm and $\lambda_2 = 530$ nm were acquired from the Michelson interferential microscope.

In all procedures to acquire interferograms, we set a tilt between the object and reference beams inside the interferometer, and it is the same for each measurement.

5.3 EXPERIMENTAL RESULTS

Having three set of non-uniform phase-shifting interferograms measured at single wavelength $\lambda_1 = 660$ nm, we computed three phases $\hat{\phi}_1$, $\hat{\phi}_2$, and $\hat{\phi}_3$ using the nine-frame PSA, one for each set of interferograms.

Estimated phase $\hat{\phi}_1$ is shown in Fig. 5.1(a). Whereas phase-sum $\hat{\phi}_{S2} = \hat{\phi}_1 + \hat{\phi}_2$ and $\hat{\phi}_{S3} = \hat{\phi}_1 + \hat{\phi}_2 + \hat{\phi}_3$ are shown in Fig. 5.1(b) and Fig. 5.1(c), respectively. Here, $\hat{\phi}_{S2}$ and $\hat{\phi}_{S3}$ represent measured phases using synthetic wavelength of $\lambda_{S2} = \lambda_1/2 = 330$ nm and $\lambda_{S3} = \lambda_1/3 = 220$ nm. The purpose to show the three phases ($\hat{\phi}_1$, $\hat{\phi}_{S2}$, and $\hat{\phi}_{S3}$) in the same figure is to illustrate that the phase wrapping is greater while more phases are summed.

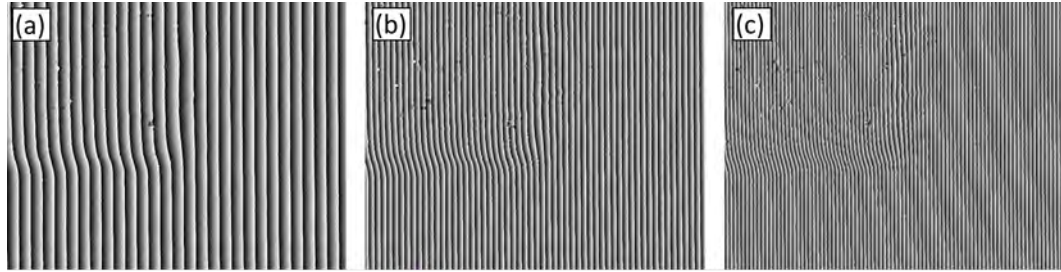


Figure 5.1: (a) Phase map measured at wavelength of $\lambda_1 = 660$ nm. Phase map measured at synthetic equivalent wavelength of (b) $\lambda_{S2} = 330$ nm, and (c) $\lambda_{S3} = 220$ nm.

In order to obtain a surface topography of an aluminum thin film with super-resolution, we use the phase-sum $\hat{\phi}_{S3}$. This result is shown in Fig. 5.2.

On the other hand, two new phases, $\hat{\phi}_4$ and $\hat{\phi}_5$, computed from two sets of interferograms at $\lambda_1 = 660$ nm and $\lambda_2 = 530$ nm are shown in Fig. 5.3(a) and Fig. 5.3(b), respectively. Whereas the phase-sum $\hat{\phi}_{S12} = \hat{\phi}_4 + \hat{\phi}_5$ is shown in 5.3(c). In these phase measurements, the spatial carrier u_0 was removed in order to illustrate the phase wrapping. Note that due to the maximum *OPD*

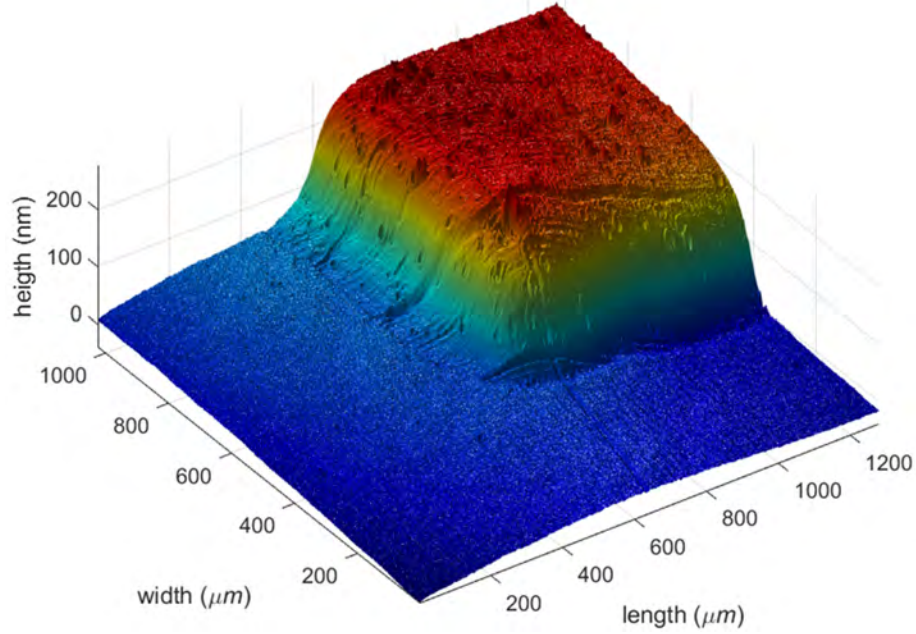


Figure 5.2: Surface topography of aluminum thin film using phase-sum at equivalent wavelength $\lambda_{eqS} = 220$ nm.

is less than $\lambda_1/2$, the phase $\hat{\phi}_4$ is not wrapped. On the contrary, phases $\hat{\phi}_5$ and $\hat{\phi}_{S12}$ are wrapped, because in these cases the maximum *OPD* is greater than $\lambda_2/2$ and $\lambda_{eqS12}/2$.

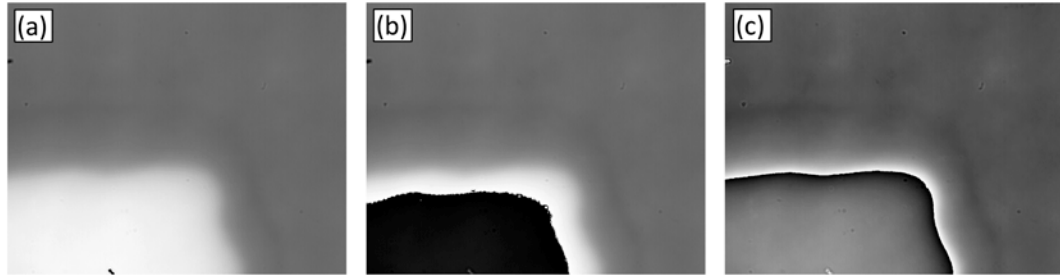


Figure 5.3: Phase map measured at wavelength of (a) $\lambda_1 = 660$ nm and (b) $\lambda_2 = 530$ nm. Phase measured at synthetic equivalent wavelength of $\lambda_{S12} = 293.95$ nm.

Surface topography of an aluminum thin film using interferograms at synthetic equivalent wavelength of $\lambda_{eqS12} = 293.95$ nm is shown in Fig. 5.4, λ_{eqS12} was computed using Eq. (5.8).

5.4 DISCUSSION

Here, we showed a surface topography of aluminum thin film with super-resolution (see Fig. 5.2), this surface was estimated using the phase-sum of three demodulated phases. Taking account that demodulated phases correspond to three different sets of non-uniform phase-shifting interferograms at $\lambda_1 = 660$ nm, the sensitivity of phase-sum is of course beyond the phase information

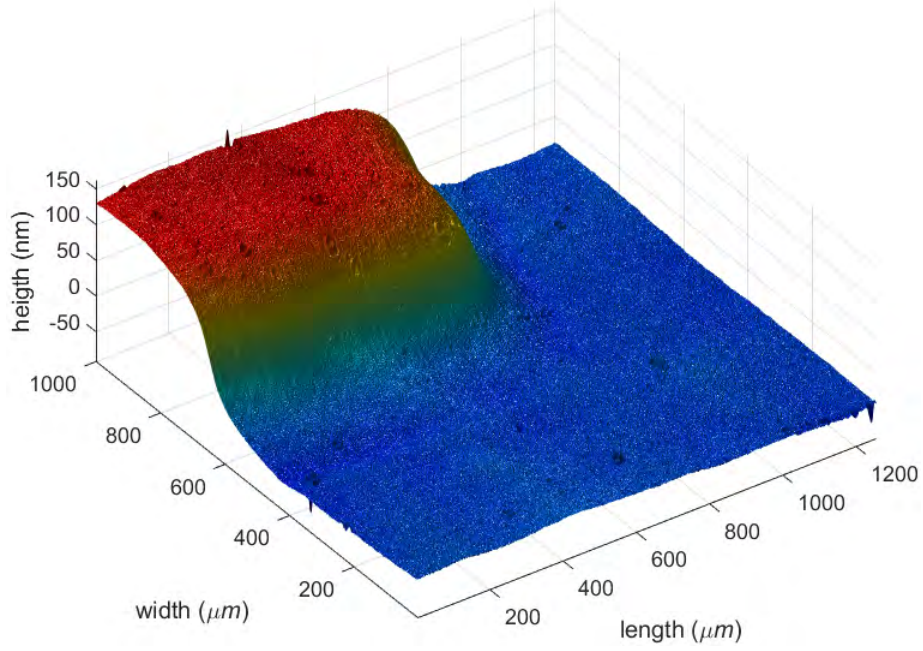


Figure 5.4: Surface topography of aluminum thin film using phase-sum at equivalent wavelength $\lambda_{eqs} = 293.95$ nm.

capacity of a single visible wavelength interferogram. Thus, $\hat{\phi}_{s2}$ simulates a phase information obtained from interferograms at ultraviolet equivalent-wavelength of $\lambda_{s3} = 220$ nm. Therefore, $\hat{\phi}_{s2}$ is three times more sensitive than $\hat{\phi}_1$, and it results in estimated surfaces with vertical super-resolution.

This ultraviolet equivalent-wavelength PSI can be extended to even higher vertical super-resolution interferometric measurements. That is to say, we can sum the demodulated phase of M visible-wavelength sets of interferograms, even using two or more different wavelengths, as we showed in Fig. 5.4. In all cases, the synthetic wavelength is always smaller than the used wavelengths to generate the interferograms.

6

Conclusions and future works

6.1 CONCLUSIONS

We illustrated the phase shifts of interferograms acquired from a Michelson interferential microscope, which use a PZT as a phase shifter. We showed two types of graphics: 1) Absolute phase shifts, where phase shifts between the n -th and the first interferogram are depicted, and 2) phase shift differences, where phase shifts between two consecutive interferograms are depicted. In both cases, non-uniform phase shifts are contrasted with uniform phase shift in order to exhibit deviation from the nominal value. Both graphics prove us that phase shift based on PZT displacement are non-uniform but not random. Consequently, it is valid to affirm that non-uniform phase shift can be expressed as the sum of the nominal value ($\omega_0 n$), a linear detuning ($\kappa_1 n$), and a quadratic detuning ($\kappa_2 n^2$).

We deduced new conditions to design PSAs in order to avoid errors in phase measurement. These errors, double-frequency ripple distortion and spurious piston, arise when interferograms with non-uniform phase shifts are demodulated using conventional PSAs. Taking account that non-uniform phase shift can be expressed as the sum of $\omega_0 n$, $\kappa_1 n$, and $\kappa_2 n^2$, we showed that conditions for eliminating these errors are associated to m -th derivative of the PSA's FTF. Hence, we establish two additional conditions: 1) the m -th derivative of the FTF evaluated at $\omega = -\omega_0$ to suppress the double-frequency ripple distortion, and 2) the m -th derivative of the FTF evaluated

at $\omega = \omega_0$ to eliminate the spurious piston.

We showed a detailed procedure to enhance the well-known four-frame PSA in order to eliminate its susceptibility to the double-frequency ripple distortion and the spurious piston. This procedure comprised two stage: 1) To conditions of the four-frame PSA, we add conditions given by the 1st and 2nd derivative of the FTF evaluated at $\omega = -\omega_0$, it result in a six-frame PSA which is robust against the double-frequency ripple distortion, and 2) To conditions of the six-frame PSA, we add conditions given by the 1st and 2nd derivative of the FTF evaluated at $\omega = \omega_0$, it result in a new eight-frame PSA whose estimated phase is error free. Simulation results prove us right. We labeled this procedure as the evolution of the four-frame PSA. In the same way, any conventional PSA can be modified in order to overcome errors produced by non-uniform phase shifts.

We designed a custom-made nine-frame PSA in order to estimate the surface topography of an aluminum thin film. This PSA was designed using the modified phase-shifting interferogram J_n , which was constructed from the non-uniform phase-shifting interferogram I_n and the measured phase shift errors (Δ_n). Nine-frame PSA includes four-frame PSA condition, to which we added the following conditions: 1) The 1st, 2nd, and 3rd derivative of the FTF evaluated at $\omega = -\pi/2$, and 2) The 1st derivative of the FTF evaluated at $\omega = \{0, \pi\}$. All of it resulted in a nine-frame PSA insensitive to the double-frequency ripple distortion. Design conditions did not include conditions for eliminating the spurious piston, because, in this specific practical measurement, this error is irrelevant.

We compared the obtained result by using the custom-made nine-frame PSA with three other methods such as: Fourier method, PCA, and least-square PSA. The obtained result from Fourier method is over smoothed, the obtained results from least-square PSA and PCA are corrupted by the double-frequency ripple distortion, whereas the surface topography profiles of an aluminum thin film is free from the double-frequency ripple distortion, and it is not over smoothed. Therefore, our propose, the custom-made nine-frame PSA, is suitable to measure thickness and roughness, as it was demonstrated graphically in Figs. 4.5 and 4.6.

We estimated the surface topography of an aluminum thin film with vertical super-resolution by using ultraviolet equivalent-wavelength PSI. To estimate this surface, we used the phase-sum which was obtained from three demodulated phases. Each demodulated phase were computed from a set of non-uniform phase-shifting interferograms, which were measured at $\lambda_1 = 660$ nm. Thus, the phase-sum simulate as if it was measured from interferograms at $\lambda_{eqsl} = 660/3$ nm, in this specific application the vertical resolution increased three times. This method is a good option to analyze roughness in surfaces under test. Nonetheless, this method can be expanded to a phase-sum of several demodulated phases, even phases computed from two or more wavelength, consequently the sensitivity of the phase-sum will increase.

6.2 FUTURE WORKS

In this dissertation, we proposed the eight-frame PSA in order to suppress the double-frequency ripple distortion and, mainly, to eliminate the spurious piston. However, we did not have the opportunity to apply this PSA in real absolute phase measurement. On the other hand, the sensitivity to random noise of this PSA is a serious problem, the signal-to-noise ratio gain (G_{SNR}) of the eight-frame PSA has to be increased. Both pending works are going to be published in following scientific papers.

We are still working in surface measurement by using synthetic ultraviolet wavelength. As we said this method is very useful to inspect roughness in surfaces with high resolution. Thus, we are planning to use phase sum which will be obtained from several sets of phase shifting interferograms. At the same time, accumulated figures of merits and the quantity of summed phases utilized to obtain the best roughness inspection will be studied in depth.

Finally, this dissertation do not pretend to give any magic PSA for phase measurement. All proposed PSAs were designed under specific conditions in order to cope our requirements. Readers should note that each experiment is different and the suitable solution can vary to each realization. And, all of it motivates us to continue searching for new PSAs which permit us more accuracy measurements in industrial, research and development applications.



The characteristic polynomial of PSAs

Any N -frame PSA can be associated with a characteristic polynomial in the Z -transform space [7, 8, 64, 65]. This polynomial is defined by

$$P(z) = \sum_{n=0}^{N-1} c_n z^n,$$

where z is a variable on the complex plane, c_n are the coefficients studied in chapter 2.3, and $P(x)$ is a polynomial of degree $N - 1$. The characteristic polynomial of a PSA usually has its roots in the complex-unit circle, and it is forbidden to have zero at the fundamental point $z = \exp(i\omega_0)$.

The characteristic polynomial provide a straightforward method to design PSAs in order to solve problems like the presence of harmonics in fringe profile, non-uniform phase shift [7], background intensity variation [8] and to investigate the effects of additive noise [64].

To exemplify the idea of the characteristic polynomial of an PSA, let us consider the four-frame PSA and the Schwider-Hariharan PSA described in section 2.3, so the characteristic polynomials of these PSAs are given by

$$P_{ff}(z) = 1 - iz - z^2 + iz^3, \tag{A.1}$$

$$P_{SH}(z) = 1 - 2iz - 2z^2 + 2iz^3 + z^4. \tag{A.2}$$

To represent the location of the roots of $P(z)$ on the complex unit circle, a characteristic diagram is employed. The corresponding diagrams of the four-frame PSA and Schwider-Hariharan PSA are displayed in Figs. A.1(a) and A.1(b), respectively. In the case of $P_{SH}(z)$, multiple roots are indicated by a blue dot surrounded by a circle.

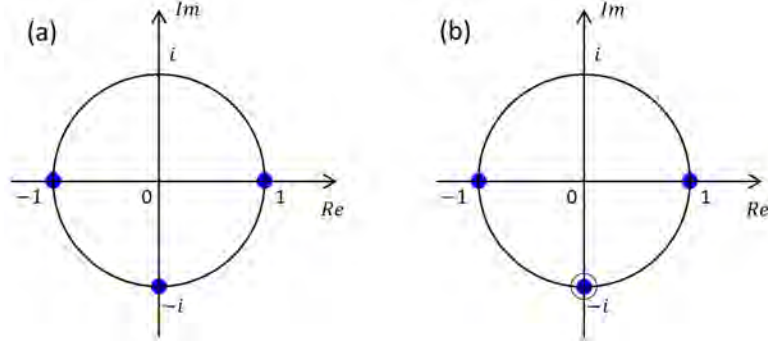


Figure A.1: Roots position of (a) the Four-Frame PSA and (b) the Schwider-Hariharan PSA.

It is stated that a PSA has its roots in the complex-unit circle, as shown in Fig. A.1. However, this is not always true, Hibino *et al.* [24] and Choque *et al.* [48] shows that roots along the complex-unit circle are useful to eliminate spurious piston in phase measurement.

B

Phase unwrapping

The phase computed as the argument of the analytic signal $(\hat{b}/2) \exp[i\hat{\phi}(x)]$ is indeterminate to a factor of 2π , and it is known as wrapped phase. This problem occurs because the angle of this analytic signal is computed by means of the arctan function, and this function is defined within $[-\pi, \pi]$ rad. This arctan operator can be considered as a wrapping operator \mathcal{W} [43, 66]. So, in order to pass the searched phase $\phi(x)$ modulo 2π to a continuous signal is necessary to use a *phase unwrapping algorithm*.

In the absence of noise, the unwrapping process is straightforward, discontinuities can be corrected by adding or subtracting the appropriate multiple of 2π [50, 67]. However, in practical measurement, there is always some amount of noise in the computed wrapped phase, in those cases, a more robust approach is required, such as quality maps, path-following and minimum-norm methods [66].

The first and most basic phase unwrapping method is the line integration of wrapped phase differences proposed by Itoh [68], a modified version of this method was proposed by Estrada *et al.* [69]. This new version result in a recursive low-pass filter/unwrapper system, which is given by

$$\hat{\phi}(x) = \hat{\phi}(x-1) + \tau \mathcal{W}[\phi_{\mathcal{W}}(x) - \hat{\phi}(x-1)]. \quad (\text{B.1})$$

In this equation, $\hat{\phi}(x)$ is the estimated unwrapped phase, $\hat{\phi}(x-1)$ represent the previous un-

wrapped site, $\phi_w(x)$ is the wrapped phase, and τ is related to the bandwidth of the low-pass filtering. This procedure can be expanded to two-dimensional phase unwrapping.

Figure B.1 show schematically the phase unwrapping process, in this example, the specimen wrapped phase is one to similar to the measured phase by using six-frame PSA.

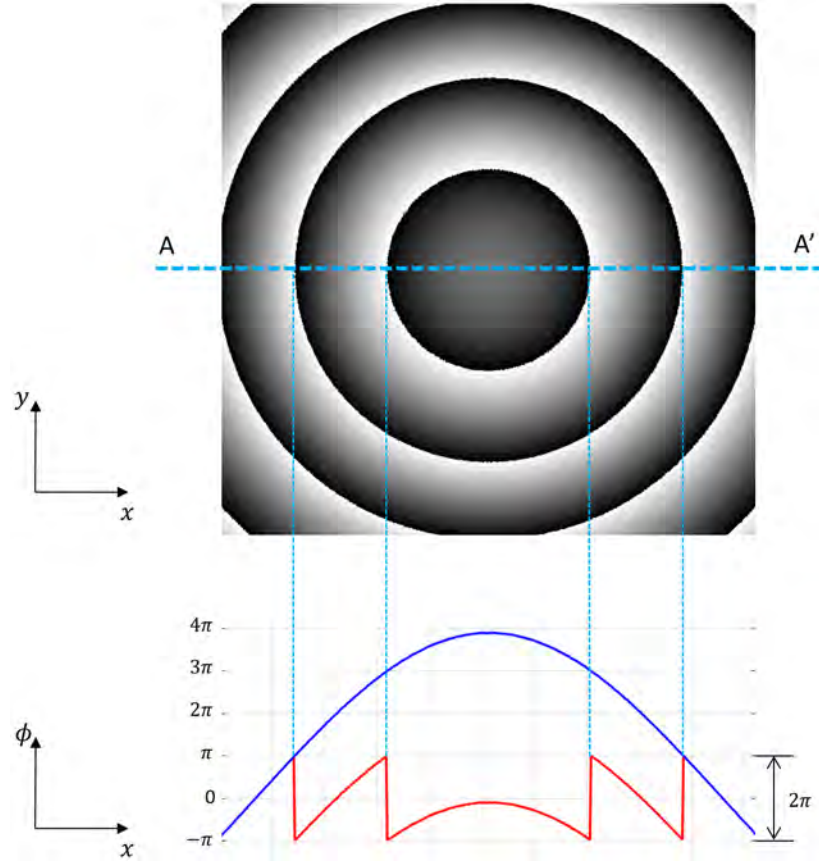
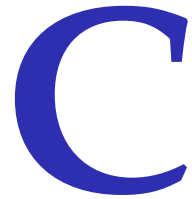


Figure B.1: Phase unwrapping in fringe analysis. In red line the wrapped phase and in blue line the unwrapped phase.

Phase unwrapping is the last step of data analysis of most interferogram analysis. To date, phase unwrapping is a matter of study and a lot of papers are still publishing.



Published material

Partial and final results contained in chapters 3 and 4 of this dissertation have been published in the following journal articles:

FIRST AUTHOR:

- **I. Choque**, M. Servin, M. Padilla, M. Asmad, and S. Ordonez, “Suppressing ripple distortions and spurious pistons in phase-shifting interferometry,” [J. Opt. Soc. Am. A](#) 37(4), 614-620 (2020).
- **I. Choque**, M. Servin, M. Padilla, M. Asmad, and S. Ordonez, “Phase measurement of nonuniform phase shifted interferograms using frequency transfer function,” [Appl. Opt.](#) 58(15), 4157-4162 (2019).

CO-AUTHOR:

- S. Ordonez, M. Servin, M. Padilla, **I. Choque**, A. Muñoz, and J. L. Flores, “Tukey’s robust M-estimator for phase demodulation of interferograms with nonuniform shifts,” [Appl. Opt.](#) 59(20), 6224-6230 (2020).

- S. Ordonez, M. Servin, M. Padilla, **I. Choque**, J. L. Flores, and A. Muñoz, "Shape defect measurement by fringe projection profilometry and phase-shifting algorithms," [Opt. Eng.](#) 59(1), 014107 (2020).
- S. Ordonez, M. Servin, M. Padilla, A. Muñoz, J. L. Flores, and **I. Choque**, "Spectral analysis for the generalized least squares phase-shifting algorithms with harmonic robustness," [Opt. Lett.](#) 44(9), 2358-2361 (2019).
- M. Servin, M. Padilla, **I. Choque**, and S. Ordonez, "Phase-stepping algorithms for synchronous demodulation of nonlinear phase-shifted fringes," [Opt. Express](#) 27(4), 5824-5834 (2019).

The final version of the last published article (as first author) was presented in the SPIE Optics + Photonics 2020 meeting, it resulted in the following proceeding:

- **I. Choque**, Moises Padilla, Manuel Servin, Sotero Ordonez, and Miguel Asmad "Suppressing ripple distortions and spurious pistons in phase-shifting interferometry", [Proc. SPIE 11490](#), Interferometry XX, 1149006 (21 August 2020).

References

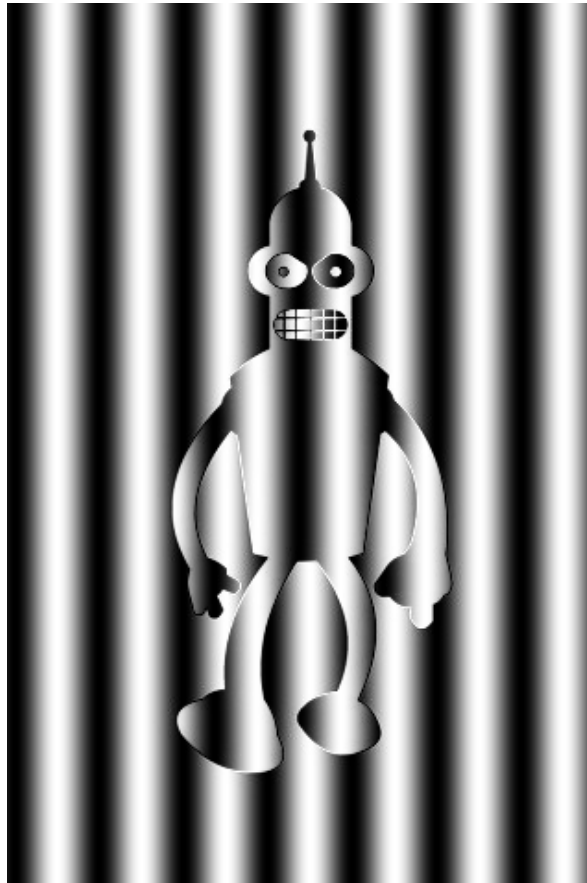
1. Bruning, J. H. *et al.* Digital wavefront measuring interferometer for testing optical surfaces and lenses. *Applied Optics* **13**, 2693–2703 (1974).
2. Wyant, J. C. Use of an ac heterodyne lateral shear interferometer with real-time wavefront correction systems. *Applied Optics* **14**, 2622–2626 (1975).
3. Schwider, J. *et al.* Digital wave-front measuring interferometry: some systematic error sources. *Applied Optics* **22**, 3421–3432 (1983).
4. Hariharan, P., Oreb, B. & Eiju, T. Digital phase-shifting interferometry: a simple error-compensating phase calculation algorithm. *Applied Optics* **26**, 2504–2506 (1987).
5. Schmit, J. & Creath, K. Extended averaging technique for derivation of error-compensating algorithms in phase-shifting interferometry. *Applied Optics* **34**, 3610–3619 (1995).
6. De Groot, P. Derivation of algorithms for phase-shifting interferometry using the concept of a data-sampling window. *Applied Optics* **34**, 4723–4730 (1995).
7. Surrel, Y. Design of algorithms for phase measurements by the use of phase stepping. *Applied Optics* **35**, 51–60 (1996).
8. Surrel, Y. Design of phase-detection algorithms insensitive to bias modulation. *Applied Optics* **36**, 805–807 (1997).
9. Hibino, K. Susceptibility of systematic error-compensating algorithms to random noise in phase-shifting interferometry. *Applied Optics* **36**, 2084–2093 (1997).
10. Hibino, K., Oreb, B. F., Farrant, D. I. & Larkin, K. G. Phase-shifting algorithms for non-linear and spatially nonuniform phase shifts. *Journal of the Optical Society of America A* **14**, 918–930 (1997).
11. Ai, C. & Wyant, J. C. Effect of piezoelectric transducer nonlinearity on phase shift interferometry. *Applied Optics* **26**, 1112–1116 (1987).
12. Cheng, Y.-Y. & Wyant, J. C. Two-wavelength phase shifting interferometry. *Applied Optics* **23**, 4539–4543 (1984).

13. Ionita, B. F., Garoi, F., Logofatu, P. C. & Apostol, D. PZT calibration. *Optik-International Journal for Light and Electron Optics* **124**, 2803–2806 (2013).
14. Panda, P. & Sahoo, B. PZT to lead free piezo ceramics: a review. *Ferroelectrics* **474**, 128–143 (2015).
15. Stone, J. A. & Zimmerman, J. H. *Index of Refraction of Air* <https://emtoolbox.nist.gov/Wavelength/Documentation.asp>. (accessed: 24.05.2020).
16. De Groot, P. J. Vibration in phase-shifting interferometry. *Journal of the Optical Society of America A* **12**, 354–365 (1995).
17. De Groot, P. J. & Deck, L. L. Numerical simulations of vibration in phase-shifting interferometry. *Applied Optics* **35**, 2172–2178 (1996).
18. Huntley, J. Suppression of phase errors from vibration in phase-shifting interferometry. *Journal of the Optical Society of America A* **15**, 2233–2241 (1998).
19. Zhao, C. & Burge, J. H. Vibration-compensated interferometer for surface metrology. *Applied Optics* **40**, 6215–6222 (2001).
20. Deck, L. L. *Suppressing vibration errors in phase-shifting interferometry* in *Advances in Metrology for X-Ray and EUV Optics II* **6704** (2007), 670402.
21. Deck, L. L. Suppressing phase errors from vibration in phase-shifting interferometry. *Applied Optics* **48**, 3948–3960 (2009).
22. Kim, Y., Hibino, K., Sugita, N. & Mitsuishi, M. Simultaneous measurement of surface shape and optical thickness using wavelength tuning and a polynomial window function. *Optics Express* **23**, 32869–32880 (2015).
23. Hibino, K. Phase-shifting algorithm inside an optical cavity for absolute length measurement. *Applied Optics* **55**, 1101–1106 (2016).
24. Hibino, K. & Kim, Y. Canceling the momentum in a phase-shifting algorithm to eliminate spatially uniform errors. *Applied Optics* **55**, 6331–6335 (2016).
25. Creath, K. *Phase-measurement interferometry: beware these errors* in *Laser Interferometry IV: Computer-Aided Interferometry* **1553** (1992), 213–220.
26. Choque, I., Servin, M., Padilla, M., Asmad, M. & Ordonez, S. Phase measurement of nonuniform phase-shifted interferograms using the frequency transfer function. *Applied Optics* **58**, 4157–4162 (2019).
27. Vargas, J., Quiroga, J. A. & Belenguer, T. Phase-shifting interferometry based on principal component analysis. *Optics Letters* **36**, 1326–1328 (2011).

28. Vargas, J., Quiroga, J. A. & Belenguer, T. Analysis of the principal component algorithm in phase-shifting interferometry. *Optics Letters* **36**, 2215–2217 (2011).
29. Du, Y., Feng, G., Li, H., Vargas, J. & Zhou, S. Spatial carrier phase-shifting algorithm based on principal component analysis method. *Optics Express* **20**, 16471–16479 (2012).
30. Vargas, J. & Sorzano, C. Quadrature component analysis for interferometry. *Optics and Lasers in Engineering* **51**, 637–641 (2013).
31. Wang, Z. & Han, B. Advanced iterative algorithm for phase extraction of randomly phase-shifted interferograms. *Optics Letters* **29**, 1671–1673 (2004).
32. Escobar, M. A., Estrada, J. C. & Vargas, J. Phase-shifting via factorization for interferometry. *Optics and Lasers in Engineering* **124**, 105797 (2020).
33. Servin, M., Padilla, M., Choque, I. & Ordonez, S. Phase-stepping algorithms for synchronous demodulation of nonlinear phase-shifted fringes. *Optics Express* **27**, 5824–5834 (2019).
34. Hibino, K. *et al.* Simultaneous measurement of surface shape and absolute optical thickness of a glass plate by wavelength tuning phase-shifting interferometry. *Optical Review* **19**, 247–253 (2012).
35. Bartl, G. *et al.* Volume determination of the Avogadro spheres of highly enriched ²⁸Si with a spherical Fizeau interferometer. *Metrologia* **48**, S96 (2011).
36. H. Komatsu, T. J. F. & Davidson, M. W. *Two-beam interferometry: Principles and Applications of Two-Beam Interferometry* <https://www.microscopyu.com/microscopy-basics/two-beam-interferometry>. (accessed: 01.04.2020).
37. Wyant, J. C. Dynamic interferometry. *Optics and Photonics News* **14**, 36–41 (2003).
38. Born, M. & Wolf, E. *Principles of optics: electromagnetic theory of propagation, interference and diffraction of light* (Cambridge University Press, Cambridge, United Kingdom, 2006).
39. Pedrotti, F. L., Pedrotti, L. M. & Pedrotti, L. S. *Introduction to optics* (Prentice Hall, 2007).
40. Sharma, K. K. *Optics: principles and applications* (Elsevier, 2006).
41. Malacara, D., Malacara, Z. & Servin, M. *Interferogram analysis for optical testing* (CRC press, 2005).
42. Hecht, E. *et al.* *Optics* (Addison Wesley San Francisco, 2002).
43. Servin, M., Quiroga, J. A. & Padilla, M. *Fringe pattern analysis for optical metrology: theory, algorithms, and applications* (John Wiley & Sons, 2014).
44. Goodwin, E. P. & Wyant, J. C. *Field guide to interferometric optical testing* in (2006).

45. Cheng, Y.-Y. & Wyant, J. C. Phase shifter calibration in phase-shifting interferometry. *Applied Optics* **24**, 3049–3052 (1985).
46. Wyant, J. C. Computerized interferometric surface measurements. *Applied Optics* **52**, 1–8 (2013).
47. Weisstein, E. W. *Maclaurin Series*, from *MathWorld* <https://mathworld.wolfram.com/MaclaurinSeries.html>. (accessed: 24.05.2020).
48. Choque, I., Padilla, M., Servin, M., Asmad, M. & Ordonez, S. Suppressing ripple distortions and spurious pistons in phase-shifting interferometry. *Journal of the Optical Society of America A* **37**, 614–620 (2020).
49. Choque, I. *Determinación de la topografía superficial de películas delgadas de TiO₂ y SiC mediante interferometría tipo Michelson* (Pontificia Universidad Católica del Perú, 2016).
50. Takeda, M., Ina, H. & Kobayashi, S. Fourier-transform method of fringe-pattern analysis for computer-based topography and interferometry. *Journal of the Optical Society of America A* **72**, 156–160 (1982).
51. Takeda, M. Fourier fringe analysis and its application to metrology of extreme physical phenomena: a review. *Applied Optics* **52**, 20–29 (2013).
52. Kreis, T. *Handbook of holographic interferometry* (2005).
53. Bertotti, F. L., Hara, M. S. & Abatti, P. J. A simple method to measure phase difference between sinusoidal signals. *Review of Scientific Instruments* **81**, 115106 (2010).
54. Liu, Y.-Z. & Zhao, B. Phase-shift correlation method for accurate phase difference estimation in range finder. *Applied Optics* **54**, 3470–3477 (2015).
55. Farrell, C. & Player, M. Phase step measurement and variable step algorithms in phase-shifting interferometry. *Measurement Science and Technology* **3**, 953 (1992).
56. Larkin, K. G. A self-calibrating phase-shifting algorithm based on the natural demodulation of two-dimensional fringe patterns. *Optics Express* **9**, 236–253 (2001).
57. Schmit, J. & Creath, K. Window function influence on phase error in phase-shifting algorithms. *Applied Optics* **35**, 5642–5649 (1996).
58. Wyant, J. Testing aspherics using two-wavelength holography. *Applied Optics* **10**, 2113–2118 (1971).
59. Polhemus, C. Two-wavelength interferometry. *Applied Optics* **12**, 2071–2074 (1973).
60. Cheng, Y.-Y. & Wyant, J. C. Multiple-wavelength phase-shifting interferometry. *Applied Optics* **24**, 804–807 (1985).

61. Creath, K., Cheng, Y.-Y. & Wyant, J. C. Contouring aspheric surfaces using two-wavelength phase-shifting interferometry. *Optica Acta: International Journal of Optics* **32**, 1455–1464 (1985).
62. Servin, M., Padilla, M. & Garnica, G. Super-resolution far-ultraviolet equivalent-wavelength interferometry combining the phase of several visible-wavelength interferograms. *arXiv preprint arXiv:1704.04700* (2017).
63. Servin, M., Padilla, M. & Garnica, G. Super-sensitive two-wavelength fringe projection profilometry with 2-sensitivities temporal unwrapping. *Optics and Lasers in Engineering* **106**, 68–74 (2018).
64. Surrel, Y. Additive noise effect in digital phase detection. *Applied Optics* **36**, 271–276 (1997).
65. Surrel, Y. Phase-shifting algorithms for nonlinear and spatially nonuniform phase shifts: comment. *Journal of the Optical Society of America A* **15**, 1227–1233 (1998).
66. Ghiglia, D. C. & Pritt, M. D. *Two-dimensional phase unwrapping: theory, algorithms, and software* (Wiley New York, 1998).
67. Yoshizawa, T. *Handbook of optical metrology: Principles and Applications* (CRC Press, 2017).
68. Itoh, K. Analysis of the phase unwrapping algorithm. *Applied Optics* **21**, 2470–2470 (1982).
69. Estrada, J. C., Servin, M. & Quiroga, J. A. Noise robust linear dynamic system for phase unwrapping and smoothing. *Optics Express* **19**, 5126–5133 (2011).



THE BASIC IDEA of a phase shifting algorithm (PSA) is to demodulate the phase from three or more phase shifting interferograms. When the phase shift is known and constant, e. g. $\pi/2$, each interferogram can be represented mathematically by an equation with three unknown variables. Then, having three phase shifted interferograms we can easily solve this equation system to obtain the searched phase. This I just explained in about three minutes is a PSA. Nonetheless, I have a Ph.D. major in this subject. [M. Servin](#)